Ocean Engineering 265 (2022) 112548

Contents lists available at ScienceDirect

Ocean Engineering

journal homepage: www.elsevier.com/locate/oceaneng

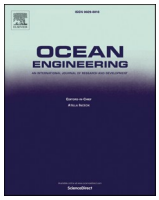

Influences of floating ice on the vertical water entry process of a trans-media projectile at high speeds

Hao Wang [a], Zhengui Huang [a,*], Ding Huang [b], Yu Hou [c], Zhihua Chen [a], Zeqing Guo [a], Shuai Sun [a], Renyuxin Xue [d]

[a] National Key Laboratory of Transient Physics, Nanjing University of Science and Technology, Nanjing, 210094, China
[b] China Academy of Launch Vehicle Technology, Beijing, 100076, China
[c] School of Electrical Engineering, Nantong University, Nantong, 226019, China
[d] Intelligent Equipment Technology Institute of Xinxing Cathay International Group, Beijing, 100020, China

ARTICLE INFO

Keywords:
Trans-media projectile
Floating ice
High-speed water entry
Supercavity
Jet flow

ABSTRACT

It is of great significance to study the hydrodynamic process of trans-media projectiles passing through ice-water mixture at high speeds for the application of weapons in low-temperature environments of high-latitude water areas during the winter. Based on the volume of fluid (VOF) method and the Schnerr-Sauer cavitation model, the processes of a projectile vertically entering water (without floating ice) and passing through ice-water mixture without collision with ice at different initial high speeds were studied. The influences caused by the ice on the cavity evolution, flow field characteristics, hydrodynamic and ballistic characteristics were analyzed. The results showed that the floating ice alters the volume of air that is sucked into the cavity by hindering the diffusion and contraction movement of the liquid at the gas-liquid interface, changing the degree of cavitation and the formation and development modes of the cavity. It causes a different evolution of the cavity shape, delays the cavity closure, and affects the hydrodynamic force and ballistic characteristics of the projectile ultimately. With increasing velocity, the influence of ice on cavity shape reduces, however, on projectile ballistics, it enhances. The results can provide some theoretical references for further application research on trans-media weapons in floating ice environments.

1. Introduction

Since the beginning of the 21st century, human emissions of greenhouse gases have continued to increase, resulting in increasingly severe global warming and the gradual melting of polar glaciers (Zhao et al., 2006; Nam et al., 2013). Large amounts of ice cover have melted into floating ice. Nearly 70% of the developed Arctic shipping lanes are covered by floating ice, so floating ice is a natural factor that cannot be ignored in the polar regions (Toyota et al., 2011). Furthermore, worldwide watersheds above 30 °N are subject to varying degrees of icing in winter (Rokaya et al., 2018), such as the Yellow Sea and the Bohai Sea, which can freeze in winter due to frequent strong cold waves, with icing periods of one to two months or even longer (Chen and Chen, 2021). Therefore, it is necessary to consider the particular situation that the primary combat environment of trans-media weapons in low-temperature environments is ice-water mixture. The trans-media projectile is a new type of marine weaponry that can effectively strike small underwater targets such as UUVs and frogmen. However, floating ice at the water surface makes the flow field of water entry more complex, resulting in more intense interference to the motion state of the projectile. Therefore, it is necessary to carry out mechanistic research on the evolution of cavity shape, hydrodynamics, and ballistic characteristics in the process of a trans-media projectile passing through ice-water mixture at high speeds.

The process of a trans-media projectile entering water at high speeds involves complex water/aerodynamic phenomena, such as water-entry impact, high-speed jet, phase translation, turbulence, and multiscale vortices. All of these have strong unsteady coupling characteristics (Wu et al., 2005; Huang et al., 2013). The research methods employed to solve the problem of high-speed water entry of projectiles can be classified into three categories: theory, numerical simulation and experiment. Back in the 1960s, Logvinovich (1969) proposed the first theory to systematically predict the expansion form of the cavity based on the potential flow theory, revealing that the expansion law of the cavity

* Corresponding author.
E-mail address: hzgkeylab@njust.edu.cn (Z. Huang).

https://doi.org/10.1016/j.oceaneng.2022.112548
Received 6 July 2022; Received in revised form 9 September 2022; Accepted 11 September 2022

crosssection is only related to the conditions at the birth time, providing a simple and effective research method for the cavity flow problem. Based on the energy conservation equation and neglect of the viscous heat generated by the motion, Lee et al. (1997) investigated the cavity generation, development, and closure processes of a high-speed projectile entering water, and established dynamic equations and a prediction model of the cavity pattern for high-speed projectiles entering water. Mirzaei et al. (2020a, 2020b) considered the cavity memory effect in conjunction with semi-empirical formulas to establish a prediction model of the cavity pattern for a cylinder entering water and calculated the hydrodynamic force of the cylinder entering water under the influence of gravity using the slicing method, which had high accuracy compared with the experimental results (Jiang and Li, 2014; Hou et al., 2018; Chen et al., 2019b).

The highly non-linear characteristics of the hydrodynamics of an object entering water make accurate description difficult using only theoretical models. Therefore, high-precision and high-speed camera technologies have been gradually employed to carry out experimental studies for high-speed water entry. Truscott et al. (2009) conducted experiments on projectiles entering water at a slight angle and a high speed (380 m/s), and explained vital issues such as the cavity generation mechanism, ballistic characteristics, and forces of the projectile. A further study by Truscott et al. (2014) comprehensively summarized the theoretical models, experimental results, and numerical analysis of water entry of objects obtained by different scholars; (Chen et al., 2019b) carried out experiments on the high-speed water entry of projectiles (44–150 m/s) and obtained laws on the influences of different head types, entry velocities, and entry angles on the ballistic characteristics and underwater pressure wave peak value. Zhao et al. (2016) investigated the oblique water-entry processes of three different head shapes of projectiles with initial velocities ranging from 50–242.6 m/s and found that the turning point of the projectile velocity curve is related to the surface closure of the cavity. A high-speed oblique water-entry experiment of a projectile (642–653 m/s) was carried out by us (Hou et al., 2020). The experimental results showed that the ballistic characteristics and underwater pressure wave variation are closely related to the sideslip angle. Sui et al. (2021) conducted an experimental study on the oblique water entry of truncated cone projectiles (41 m/s) with 40 different head shapes and discovered a quantitative relationship between the peak load and the truncated cone geometric shape. Lyu et al. (2021) investigated the influence of the time interval of two tandem spheres entering water vertically (15–45 m/s) on the evolution of the cavity and quantified the relationship between the cavitation characteristics and Froude number (Fr). The results showed that the accelerated decay rate of the second sphere decreases with the increase in the ratio of the time interval between the two spheres and the deep pinch-off time of the second cavity. Besides, the cavity evolution of two spheres in tandem vertically entering water at different Fr (2.5–50) was also studied (Lyu et al., 2022). It was found that the latter sphere has three typical water-entry modes, and all of them can reduce the drag force.

Due to experimental equipment limitations and the difficulty in precisely measuring the underwater parameters, it is difficult to conduct high-precision experimental research on the problem of high-speed water entry of objects under complex conditions. With the rapid development and maturity of computer technology, numerical simulation has become an essential tool for studying high-speed water-entry problems and has been widely used (Rand et al., 1997; Kirschner et al., 2002). Compared with experimental and theoretical methods, numerical simulation can provide more precise information about the flow characteristics, such as pressure and velocity fields, revealing the interaction between the water, vapor and projectile. Jiang et al. (2016) calculated the processes of a projectile vertically entering the water with a drag-reducing additive at 28.4–142.7 m/s. The results showed that the drag-reducing additive can promote cavitation and lengthen the cavity, thereby reducing drag force. (Chen et al., 2019a) conducted a numerical simulation of a high-speed oblique water entry process (70 m/s) of a vehicle with various entry angles, entry speeds, and cavitator areas, finding that the peak force dimensionless coefficient of the vehicle entry load is independent of the entry speed and cavitator area. Mu et al. (2020) investigated the process of high-speed inclined water entry (300 m/s) of cylinders with different densities and analyzed the cavity shape and the motion characteristics of the cylinder under the influence of density. Lu et al. (2021) numerically calculated the high-speed parallel water entry of projectiles (280–400 m/s) and investigated the influences of different entry speeds and the space between projectiles on the flow field characteristics, ballistic stability, and drag reduction characteristics, discovering that the parallel projectile is subjected to greater lateral force, and the drag reduction effect decreases as the projectile spacing decreases.

To sum up, the current research on the problem of high-speed water entry focuses primarily on different projectile structures, entry angles, and speeds in pure water environments, with little attention to the cases of objects entering complex water environments where solid obstacles exist. Zhang et al. (2020) and Cai et al. (2020) used the ALE method to numerically study the process of a slender vehicle launched underwater penetrating ice-water mixture (20 m/s). The results showed that the motion trajectory of the vehicle is deviated by the impact of floating ice, and the influences of different ice distribution forms and initial relative exit positions on the displacement of the vehicle centroid and flow field characteristics vary. The experimental (3.91–5.57 m/s) and numerical simulation studies (25 m/s) of a slender vehicle obliquely launched underwater passing through ice-water mixture were carried out by Zhang et al. (2021) and You et al. (2022), respectively. The results revealed that the effect of the floating ice on the flow field characteristics is primarily related to the intensity and extent of the splash caused by cavity collapse, and that the floating ice causes significant fluctuations in the pressure of the vehicle surface, which deviates the motion trajectory. Ren and Zhao (2021) established a three-dimensional ice--water-structure interaction model to calculate the low-speed ice-breaking water entry process (3.43 m/s) of a rigid ball, and analyzed the crack expansion path of the ice cover, cavity shape, and flow field characteristics. The influences of varying ice thicknesses, ice elastic moduli, water-entry speeds and sphere densities on the ballistic trajectory of the sphere were also discussed. We (Wang et al., 2022) investigated the processes of a cylinder vertically entering water (without floating ice) and ice-water mixture (4.2 m/s) based on the VOF model, respectively. The results indicated that the floating ice changes the initial splash shape, leading to the absence of the surface closure of the cavity, resulting in a pressure difference change inside and outside of the cavity, which significantly influences the characteristics of flow fields. It can be seen that the current research on objects passing through ice-water mixture is limited to low speeds, with little research on high-speed projectiles passing through ice-water mixture without collision. Trans-media projectiles in polar low-temperature conditions face an exceptional mechanical environment, and the effects of floating ice on the vertical water entry of a high-speed projectile at different speeds are still unknown.

The experimental conditions of a high-speed trans-media projectile passing through ice-water mixture at a low temperature are incredibly harsh, so the numerical simulation method has become an effective method for this study. In this study, the processes of the projectile with initial velocities of 100 m/s, 200 m/s, 400 m/s, and 500 m/s entering water vertically (without floating ice) and passing through ice-water mixture (without collision with floating ice) were numerically simulated. The influence mechanism of free-moving floating ice on the evolution of the water-entry cavity and the proportion of fluid in each phase of the cavity was analyzed. In addition, there is an in-depth discussion on the influences of floating ice on the water-entry flow fields, hydrodynamic force, and trajectory characteristics, which can provide a theoretical reference for the application research of trans-media weapons in extremely low-temperature environments.

2. Numerical methods

2.1. Governing equations

The speed of the projectile entering water is less than 700 m/s, the flow barely influences the temperature of the flow field, so the compressibility effects (Lee et al., 1997) and the energy equation are not considered in our simulations. Therefore, assuming that the fluid is incompressible homogeneous and ignoring the heat conduction effect caused by viscosity, only the mass conservation and momentum conservation equations are considered as the control equations of multiphase flow:

$$\frac{\partial \rho_m}{\partial t}+\frac{\partial(\rho_m u_i)}{\partial x_i}=0 \tag{1}$$

$$\frac{\partial(\rho_m u_i)}{\partial t}+\frac{\partial\left(\rho_m u_i u_j\right)}{\partial x_j}=-\frac{\partial P}{\partial x_i}+\mu_m \frac{\partial}{\partial x_j}\left(\frac{\partial u_i}{\partial x_j}+\frac{\partial u_j}{\partial x_i}\right)+\rho_m g_i \tag{2}$$

where ρ_m and P denote the mixture's density and flow pressure, u_i and g_i are the components of fluid velocity and gravitational acceleration in i direction in the Cartesian coordinate system, respectively. μ_m is the dynamic viscosity of the mixture.

2.2. Turbulence model

The high-speed water entry process exhibits strong transient non-constant properties and turbulent flow. SST k-ω turbulence model (Menter, 1994) can better predict wall-flow separation problems under strong adverse pressure gradients. The eddy viscosity coefficient is defined as:

$$\mu_t=\frac{\rho_m a_1 k}{\max(a_1\omega, SF_1)} \tag{3}$$

where $a_1=0.31$ is the model coefficient, k and ω are the turbulent kinetic energy and the unit dissipation rate, separately. $S=\sqrt{2S_{ij}S_{ij}}$ represents the average strain rate tensor, F_1 is a blending function calculated as follows:

$$F_1=\tanh\left\{\left[\max\left(\frac{2\sqrt{k}}{\beta^*\omega d},\frac{500v}{d^2\omega}\right)\right]^2\right\} \tag{4}$$

where $\beta^*=0.09$, d is the nearest distance from the flow field to the wall.

The transport equation for the turbulent kinetic energy k and the unit dissipation rate ω is expressed as:

$$\frac{\partial(\rho_m k)}{\partial t}+\frac{\partial(\rho_m u_i k)}{\partial x_i}=P_k-\beta^*\rho k\omega+\frac{\partial}{\partial x_i}\left[(\mu+\sigma_k\mu_t)\frac{\partial k}{\partial x_i}\right]+P_{kb} \tag{5}$$

$$\frac{\partial(\rho_m \omega)}{\partial t}+\frac{\partial(\rho_m u_i \omega)}{\partial x_i}=\alpha\frac{\omega}{k}P_k-\beta\rho\omega^2+\frac{\partial}{\partial x_i}\left[(\mu+\sigma_\omega\mu_t)\frac{\partial\omega}{\partial x_i}\right]+2(1-F_2)\rho\sigma_{\omega 2}\frac{1}{\omega}\frac{\partial k}{\partial x_i}\frac{\partial\omega}{\partial x_i}+P_\omega \tag{6}$$

where P_k and P_ω depict the generating terms considering turbulence and buoyancy, unit dissipation and cross dissipation, respectively. σ_k and σ_ω are the model coefficients associated with the blending function F_2, which are presented as follows:

$$\sigma_k=F_2\sigma_{k1}+(1-F_2)\sigma_{k2} \tag{7}$$

$$\sigma_\omega=F_2\sigma_{\omega 1}+(1-F_2)\sigma_{\omega 2} \tag{8}$$

$$F_2=\tanh\left\{\left\{\min\left[\max\left(\frac{\sqrt{k}}{\beta^*\omega d},\frac{500v}{d^2\omega}\right),\frac{4\rho\sigma_{\omega 2}k}{CD_{k\omega}d^2}\right]\right\}^4\right\} \tag{9}$$

where the parameters $\sigma_{k1}=0.85$, $\sigma_{k2}=1$, $\sigma_{\omega 1}=0.5$, $\sigma_{\omega 2}=0.856$, and $CD_{k\omega}=\max\left(2\rho\sigma_{\omega 2}\frac{1}{\omega}\frac{\partial k}{\partial x_i}\frac{\partial\omega}{\partial x_i},10^{-10}\right)$ are the model coefficients.

2.3. VOF model

The volume of fluid (VOF) model is a surface tracking method based on the Euler grid on the premise that various fluids are immiscible with each other, which can effectively capture the free surface deformation. For the problem of high-speed water entry, it is necessary to consider the cavitation phenomenon caused by the low-pressure area around the projectile, involving multiphase interactions. The parameters α_l, α_g and α_v denote the volume fractions of water, air and vapor, respectively. All phases are assumed to have the same velocity and pressure field.

Fluid density and dynamic viscosity of the mixture are defined as:

$$\rho_m=\alpha_l\rho_l+\alpha_g\rho_g+\alpha_v\rho_v \tag{10}$$

$$\mu_m=\alpha_l\mu_l+\alpha_g\mu_g+\alpha_v\mu_v \tag{11}$$

where ρ_l, ρ_g, ρ_v and μ_l, μ_g, μ_v denote the density and the dynamic viscosity of water, air and vapor, respectively.

Each phase obeys the component conservation law:

$$\alpha_l+\alpha_g+\alpha_v=1 \tag{12}$$

2.4. Cavitation model

The Schnerr-Sauer cavitation model relates the volume fraction of the vapor phase to the density of bubbles in the liquid, which has the advantages of simplicity of form, robustness, and efficiency of calculation (Schnerr and Sauer, 2001), so the Schnerr-Sauer cavitation model is used to describe the cavitation phenomenon of high-speed water entry. The mass transport equation of the model is established based on the vapor phase:

$$\frac{\partial\alpha_v}{\partial t}+\frac{\partial(\alpha_v u_i)}{\partial x_j}=F_{vap}\frac{2\alpha_{nuc}(1-\alpha_v)\rho_v}{R_B}\sqrt{\frac{2}{3}\frac{p_v-p}{\rho_l}}-F_{cond}\frac{3\alpha_v\rho_v}{R_B}\sqrt{\frac{2}{3}\frac{p-p_v}{\rho_l}} \tag{13}$$

where $F_{vap}=50$, $F_{cond}=0.001$, $\alpha_{nuc}=0.0005$ is the volume fraction of non-condensable gas, $R_B=1\times10^{-6}m$ is the radius of the gas nucleus, $p_v=610.47$Pa is the saturated vapor pressure of 0 °C water.

2.5. Motion equation of six degrees of freedom body

The dynamic fluid body interaction module (DFBI) is used to calculate the forces of a six-degree-of-freedom body in the fluid domain, including gravity, inertia moment, and fluid impact force. According to the centroid motion equation and the rotation equation, the centroid position and attitude angle of the moving body for each time step can be calculated.

The centroid motion equation can be expressed as:

$$m\frac{d\boldsymbol{u}}{dt}=\boldsymbol{f} \tag{14}$$

$$\boldsymbol{f} = \boldsymbol{fp} + \boldsymbol{f\tau} + mg \tag{15}$$

where m is the mass of the moving body, $\boldsymbol{u}$ is the centroid velocity vector at time t, $\boldsymbol{f}$, $\boldsymbol{fp}$, $\boldsymbol{f\tau}$ denote the combined force, fluid pressure and fluid shear force acting on the moving body, respectively.

The rotation equation is defined as:

$$\boldsymbol{J}\frac{d\boldsymbol{\omega}}{dt} + \boldsymbol{\omega} \times \left(\boldsymbol{J} \bullet \boldsymbol{\omega}\right) = \boldsymbol{M} \tag{16}$$

$$\boldsymbol{M} = \boldsymbol{Mp} + \boldsymbol{M\tau} \tag{17}$$

where $\boldsymbol{J}$ and $\boldsymbol{\omega}$ denote rotational inertia tensor and angular velocity of the moving body, respectively. $\boldsymbol{M}$, $\boldsymbol{Mp}$ and $\boldsymbol{M\tau}$ denote the resultant moment, fluid pressure moment, and fluid shear moment acting on the centroid of the moving body, respectively.

2.6. Physical model

As shown in Fig. 1, the projectile is a cylinder. The projectile's height, diameter and weight are L=75.9 mm, D_0=12.65 mm, and m=0.026 kg, respectively. The initial water-entry velocity is 100 m/s, 200 m/s, 400 m/s and 500 m/s. Considering the size, shape, and density of the floating ice (Wang et al., 2018), a shape of thin cylinders is used to simulate the floating ice at sea level, with a density of 920 kg/m^3, a diameter of 2 D_0, and a height of D_0. Around the water entry point of the projectile, four pieces of floating ice distribute evenly. The floating ice is in a balanced state of equal buoyancy and its own gravity before the projectile enters the water. The gap between the floating ice and the projectile is D_0/8, and no collision between the floating ice and the projectile occurs during the water entry.

Because the floating ice only interacts with water during its entire movement. In the extremely short time when the high-speed projectile enters the water without collision with ice, the phase change process of floating ice is not considered. Moreover, the main concern is the influences of floating ice on the cavity shape, flow field characteristics, hydrodynamics, and ballistic characteristics of the projectile during the water-entry process. In order to simplify the computational model, regard the projectile and the floating ice as moving bodies with a constant relative distance between internal particles. Take the time when the projectile starts moving as t=0 ms. Initially, the distance between the projectile head and the water surface is D_0. Define the earth coordinate system $Ox_0y_0z_0$ and the projectile coordinate system $Oxyz$, which both take the projectile centroid as the origin to describe the projectile's motion. The x-axis of the projectile coordinate system is consistent with the direction of gravity at the initial time and vertically downward. The y-axis is parallel to the water surface, and the z-axis is perpendicular to the Oxy plane and complies with the right-hand screw rule. Each axis direction of the earth coordinate system is the same as the projectile coordinate system at the initial time.

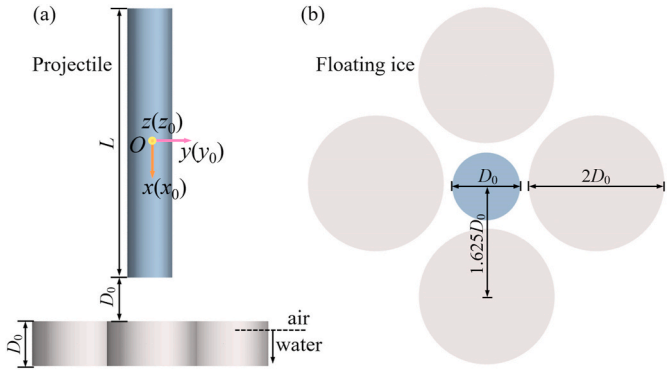

Fig. 1. Projectile and floating ice at the initial time.

Vertical water entry (no floating ice) is replaced by "only-water". The calculated environmental conditions are set to 0 °C in all cases of only-water and ice-water mixture.

The critical cavitation number σ_0 is as follows:

$$\sigma_0 = \frac{P_\infty - P_v}{\frac{1}{2}\rho_l v^2} \tag{18}$$

where $P_\infty = \rho_l gh + P_0$ is environmental pressure, $h = 0$ in the initial time state, v is the moving speed of the projectile.

The Reynolds number, a defining feature of fluid flow, is defined as:

$$Re = \frac{\rho_l v D_0}{\mu_l} \tag{19}$$

In all cases, the critical Reynolds number range is 1.255×10^6–6.274×10^6.

The Froude number describes the relative magnitudes of inertial force and gravity, is given by:

$$Fr = \frac{v^2}{gD_0} \tag{20}$$

In all cases, the critical Froude number range is 8.058×10^4–2.015×10^6, and the other initial parameters are shown in Table 1.

As shown in Fig. 2a, the geometrical dimension of the computational domain is 40 D_0 × 40 D_0 × 75 D_0. The static water surface is 25 D_0 from the top of the computational domain. Set the top section of the computational domain as the velocity inlet; the sides and bottom are the pressure outlets, and the surfaces of the projectile and the floating ice are the wall. In addition, the inlet velocity at the top section of the domain is zero. The underwater pressure changes with the water depth, adopting the user-defined function $P_\infty = \rho_l gh + P_0$, where P_0 is 101325 Pa.

Fig. 2b shows the mesh on the xoy section. Use a trimmer mesh consisting of hexahedral cells with good computational performance and a surface reconstruction to improve the mesh quality. Moreover, the mesh area near the moving bodies' walls is refined to improve the accuracy of capturing the details of the flow field at the boundary layer. The overlapping mesh nested within the background domain mesh is used to simulate the vertical water entry of the high-speed projectile. During the calculation process, the background domain mesh remains stationary, and the overlapping mesh moves in the same way as the motion of the moving body.

In the present work, the computational fluid dynamics (CFD) software STAR-CCM+ 15.02.007 was used for the simulation. The VOF model was used to simulate the immiscible fluid, and the still water VOF wave was established to represent the calm liquid surface. Used the Schnerr-Sauer cavitation model to describe the cavitation phenomenon. Six-degree-of-freedom bodies were created by the overlapping mesh and the DFBI model to simulate the projectile and floating ice. Adopted the finite volume method (FVM) to discretize the governing equations. A second-order implicit scheme was used to solve the time term, and the time step was 5×10^{-6}s to ensure that the Courant number was less than 1 to obtain the convergent solution. The convection term and diffusion term adopted the second-order upwind scheme and the second-order central difference scheme, respectively. Used the SIMPLE algorithm

Table 1
Conditions of calculation cases.

Case	Condition	Velocity	σ_0	*Re*	*Fr*
1	only-water	100 m/s	0.02	$1.255\text{x}10^6$	$8.058\text{x}10^4$
2	ice-water mixture	100 m/s	0.02	$1.255\text{x}10^6$	$8.058\text{x}10^4$
3	only-water	200 m/s	0.005	$2.510\text{x}10^6$	$3.223\text{x}10^5$
4	ice-water mixture	200 m/s	0.005	$2.510\text{x}10^6$	$3.223\text{x}10^5$
5	only-water	400 m/s	0.0013	$5.019\text{x}10^6$	$1.289\text{x}10^6$
6	ice-water mixture	400 m/s	0.0013	$5.019\text{x}10^6$	$1.289\text{x}10^6$
7	only-water	500 m/s	0.0008	$6.274\text{x}10^6$	$2.015\text{x}10^6$
8	ice-water mixture	500 m/s	0.0008	$6.274\text{x}\ 10^6$	$2.015\text{x}10^6$

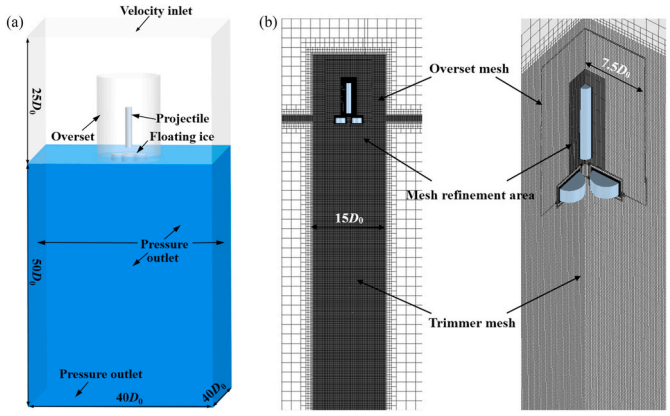

Fig. 2. Schematic of (a) the boundary conditions and (b) the mesh on the *xoy* plane.

(Semi-Implicit Method for Pressure-Linked Equations) to solve the pressure-velocity coupling. Adopted the algebraic multi-grid (AMG) linear solver to accelerate the calculation. The Gauss-Seidel method in the relaxation scheme was used to enhance the convergence of the results.

2.7. Validation of the present numerical model

An identical calculational model was established for the vertical water entry of a steel 45 cylindrical projectile with a length of 24 mm, a diameter of 6 mm, a mass of 4.88 g, and a water-entry velocity of 106.8 m/s as in the experiment done by Chen et al. (2019). Fig. 3a and Fig. 3b show the cavity shape obtained by the experimental results from the literature and the simulation using the present numerical model in this study, respectively, illustrating the whole process of initial impact, open cavity expansion, and cavity surface closure. The numerical results depict the same complex hydro-aerodynamic phenomena as the experimental results, such as the liquid surface splash and the return jet flow inside of the cavity. For quantitative comparison, select the typical cavity cross-section at 1/2 depth from the projectile head to the water surface. It follows that the cavity width is nearly constant, and the maximum error is only 0.65%. The cavity length and profile calculated in this paper are highly consistent with the experiments, and the cavity closure time and closure depth are the same.

Fig. 4a and Fig. 4b depict the velocity and displacement curves at different times. It shows that the numerical results in this paper have the same magnitude and turning trend as the experimental data. It demonstrates that the present numerical model used in this study can accurately reflect a series of development processes after the object enters the water at high speed. On this basis, a numerical study of the high-speed projectile with different initial velocities vertically entering water and passing through ice-water mixture will be carried out.

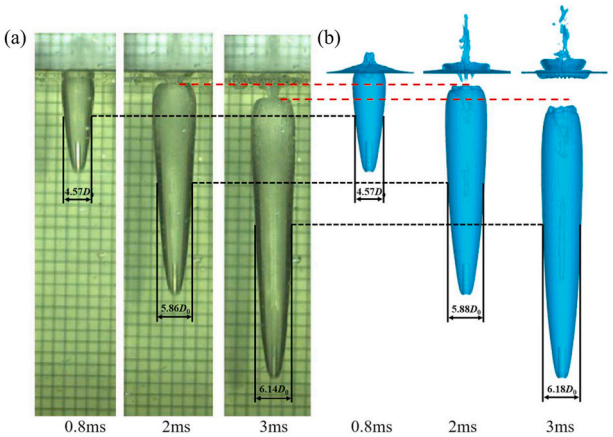

Fig. 3. Comparison of cavity evolution between (a) the experiment result and (b) the numerical simulation.

In order to exclude the influence of the grid number and the size of the boundary layer grid on the calculation results, taking Case 1 and Case 2 as examples, five different grid levels were established, i.e., 6.6 million, 7.2 million, 8.0 million, 8.9 million and 10.0 million. The first thickness of the mesh is 1.6×10^{-6} m, 7.2×10^{-7} m, 2.4×10^{-7} m, 8.1×10^{-8} m and 3.2×10^{-8} m, respectively. Fig. 5 shows the vertical acceleration of different mesh levels. During the initial impact stage, acceleration fluctuations in ice-water mixture are intense. The acceleration changes in the two cases are the same after the projectile has wholly entered the water. The curve values of the two cases under different grid levels have little difference. To ensure the results' accuracy and speed up the calculation, a grid level of 8.0 million was chosen for further simulation.

The dimensionless wall distance y^+ determines the thickness of the near-wall region. According to the y^+ formula: $y^+=(y\rho u_\tau)/\mu$, the y^+ value is proportional to the normal distance y perpendicular to the wall. Fig. 6 depicts the y^+ distribution on the projectile surface in Case 1 and Case 2. The head and shoulder of the projectile is the area concentrated with the more significant value of y^+ at the initial impact stage. Within a short period, the tail's y^+ value increases rapidly. After 2.0 ms, the y^+ value of the projectile surface except for the head is small, and the distribution of the y^+ value on the projectile surface in Case 2 is more evident than that in Case 1. Fig. 7 shows the maximum value of y^+ value on the surface of the projectile. The value of y^+ rises rapidly due to the strong interaction between the projectile head and the water surface at the initial impact stage. With the formation of open cavity, y^+ gradually decreases, and the value of y^+ in Case 2 is approximately double that in Case 1. The y^+ value of both cases is in the order of 1 during the whole water entry process, and the y^+ value corresponding to this grid level can meet the requirements of the SST k-ω turbulence model.

3. Results and discussion

3.1. Influence of floating ice on the evolution of the cavity shape

When the projectile passes through the air-water interface with or without floating ice at the same high speeds, the classification of cavity evolution stages is similar to a certain extent. After the projectile impacts the water surface and disturbs the water area, there are four stages through the whole cavity evolution process: initial impact, open cavity, cavity closure, and collapse. This process exhibits complex and regular evolution characteristics. In this section, the influence of floating ice on the evolution of cavity shape is investigated qualitatively and quantitatively. Due to the high speed of the projectile, the cavity closure can still be maintained for a long time, and the cavity collapse phase is not considered in this paper due to the limitation of the calculation resources.

3.1.1. Evolution mechanism of the cavity shape

In order to fully comprehend the influence of floating ice on the evolution law of the cavity shape, the flow field characteristics of the first three stages of cavity evolution under Case 1, 2, 5, and 6 are compared and analyzed with the initial velocities of 100 m/s and 400 m/s as examples. Fig. 8 and Fig. 9 show the three-dimensional cavity evolution processes of the projectile with different initial velocities under only-water and ice-water mixture, and the corresponding top views are shown in Fig. 10 and Fig. 11.

First, a comparative analysis of the initial impact stage of 100 m/s is carried out (0–0.4 ms, Fig. 8). In Case 1, the projectile collides with the liquid surface, transferring the kinetic and potential energy to the surrounding fluid particles. Flow separation occurs at the head of the projectile, and the cavity expands rapidly in a short time, forming an

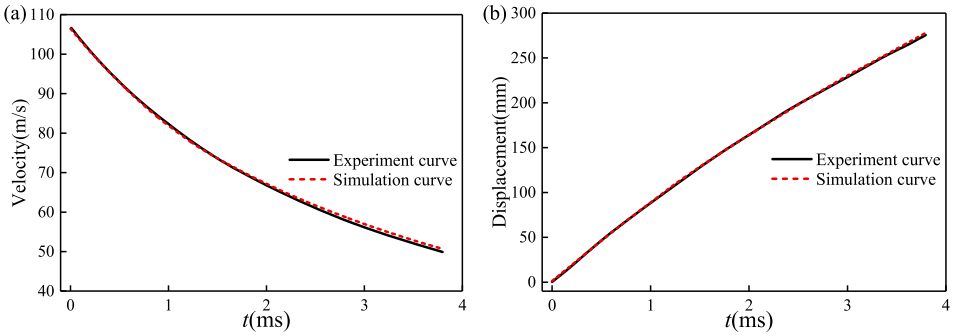

Fig. 4. Comparisons of (a) velocity and (b) displacement at different times between the experiment result and the numerical simulation.

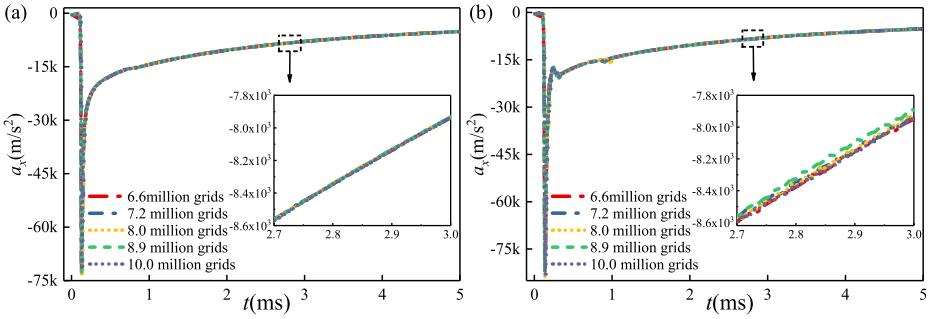

Fig. 5. Acceleration for different grid levels of (a) Case 1 and (b) Case 2.

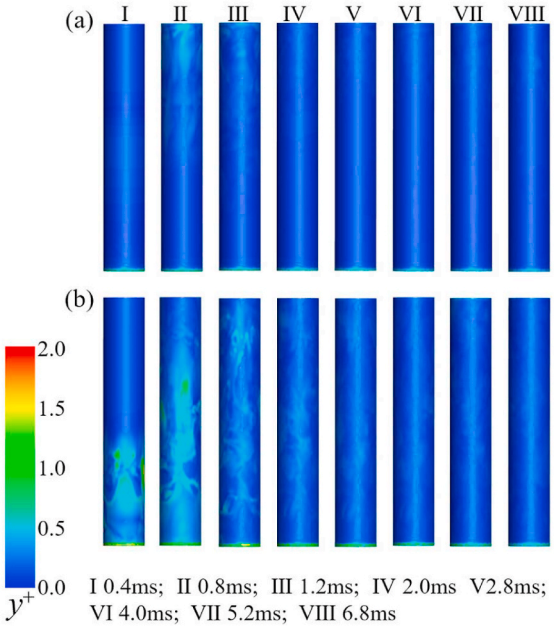

Fig. 6. The distribution of y^+ value on the projectile surface of (a) Case 1 and (b) Case 2.

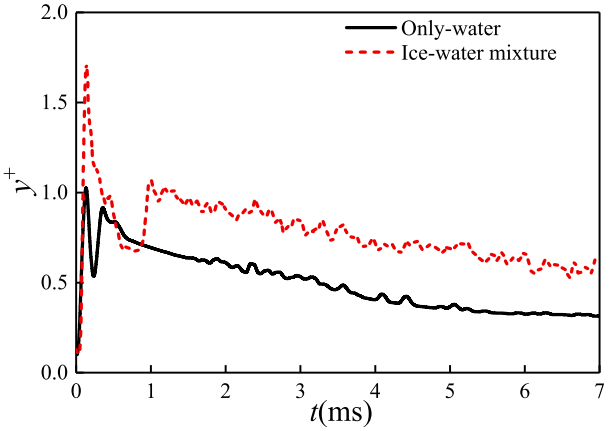

Fig. 7. The maximum value of y^+ value on the projectile surface of Case 1 and Case 2.

open cavity. The free liquid surface around the projectile rises, and the fluid kinetic energy converts into potential energy, which expands significantly along the horizontal and vertical directions to form a noticeable splash ring, which rises with the increasing depth of the projectile entering the water and has an annular-shaped symmetry.

The initial impact stage of Case 2 is shown in Fig. 8b. The floating ice hinders the air influx, resulting in a narrower cavity diameter (0.4 ms) and a smaller cavity volume around the projectile head than that of Case 1. In addition, the liquid splash phenomenon is different from Case 1 because the projectile's kinetic energy needs to convert into the kinetic energy of liquid diffusion and movement of floating ice, wherein the inertial force of the floating ice is much larger than that of water. Moreover, the initial cavity wall is at the same height as the floating ice, resulting in only a tiny portion of the liquid forming a splash. A part of the splash rises, hits the floating ice, and then flies out from the gap between the floating ice and the projectile, while the other part flies out from the gap among the floating ice bodies. Due to the extrusion of small gaps, the splash height is higher than that without floating ice. The splash ring is no longer annularly symmetric, affected by floating ice, but axisymmetrical (Fig. 10b).

Another obvious distinction between these two cases is that the shoulder of the projectile in Case 2 is wet (Fig. 8b). The formation mechanism of this phenomenon is illustrated with a two-dimensional schematic at a particular moment after the initial impact, as shown in Fig. 12. The liquid splash in only-water develops outward and upward

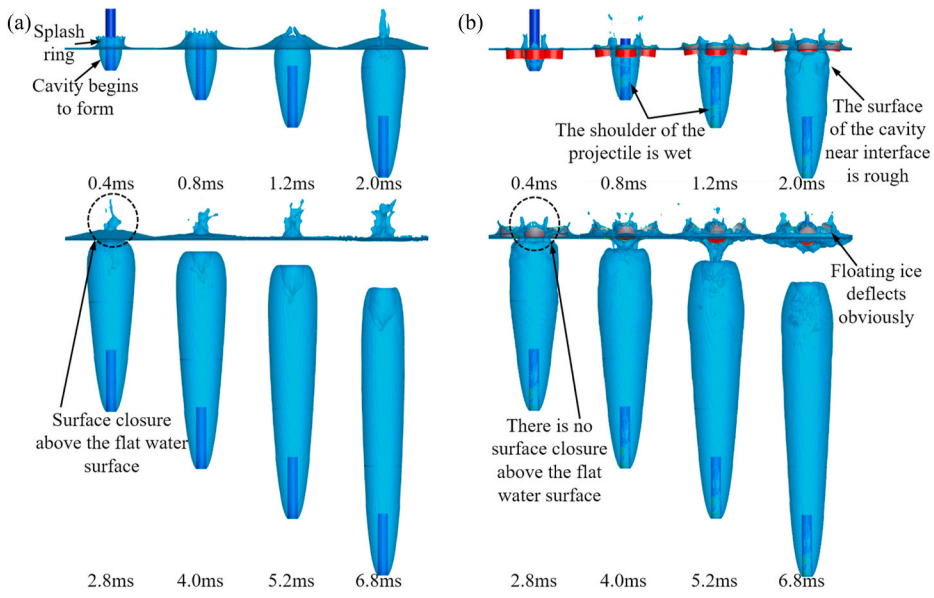

Fig. 8. Cavity evolution of (a) Case 1 and (b) Case 2 (front view).

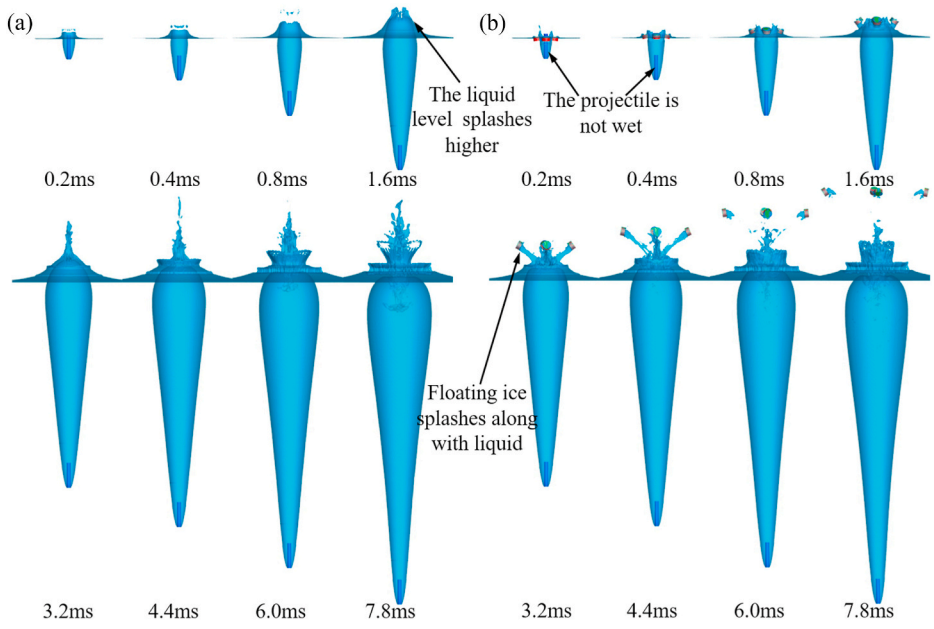

Fig. 9. Cavity evolution of (a) Case 5 and (b) Case 6 (front view).

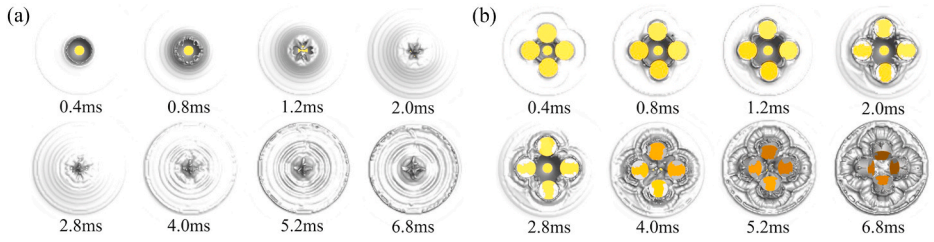

Fig. 10. Cavity evolution of (a) Case 1 and (b) Case 2 (top view).

unimpededly. However, the liquid surrounding the projectile in ice-water mixture collides with the floating ice in upward and outward movement. During the collision, the kinetic energy in the horizontal direction transmits to the floating ice, and the liquid droplet rebound caused by the collision wets the projectile.

Comparing Figs. 8 and 9, it can be found that with the increase of the initial velocity, the width and length of the cavity at the initial impact stage (0–0.2 ms) of 400 m/s increase significantly, and the higher kinetic

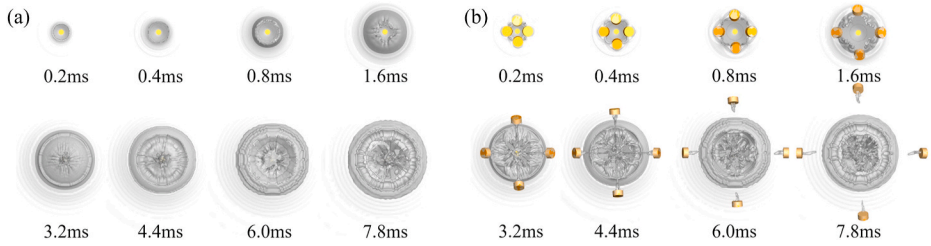

Fig. 11. Cavity evolution of (a) Case 5 and (b) Case 6 (top view).

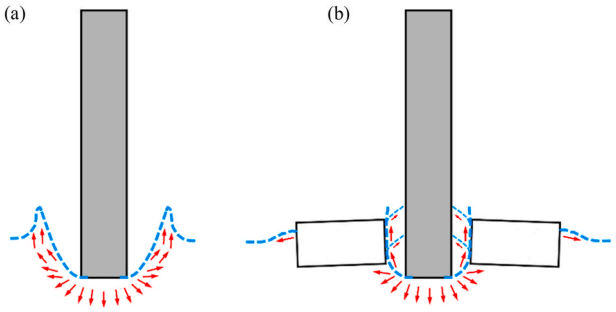

Fig. 12. Schematic diagram of cavity flow pattern at the moment of entering water of (a) Case 1 and (b) Case 2.

energy promotes the rapid outward diffusion of the floating ice in a short time. The degree of difference between the liquid surface splash in Case 5 and Case 6 reduces, and the projectile in Case 6 is not wet. The reasons for the different phenomena from Case 2 will be explained in section 3.2.

At the open cavity stage (0.4–2.0 ms, Fig. 8) of Case 1, the cavity length is continuously stretched with the downward movement of the projectile, and the width and volume of the cavity gradually increase due to the external air influx and the vapor generated by cavitation, showing a regular elliptical shape. The splash ring contracts toward the central axis and falls back (2.0 ms) due to the combined effects of surface tension, gravity, and aerodynamic forces. The contracting fluids in opposite directions collide at a certain height. Two jets of upward and downward appear at the impact point, forming a closed vaulted dome that prevents outside air entering. It is the surface closure above the calm water surface, signaling the start of the cavity closure stage (2.0–6.8 ms). As more and more fluid particles participate in the movement, the diameter of the two jets gradually increases, and the development of the cavity only depends on the vapor generated by the cavitation effect.

The deflection of floating ice can reflect the change of the water surface flow field. From Figs. 8b and 10b, the floating ice with a more significant inertia force hinders the contraction movement of the liquid surface, which substantially prolongs the cavity opening time, so the duration of the open cavity stage in Case 2 (0.4–6.8 ms) is four times longer than that of Case 1 (0.4–2.0 ms). During the period from 0.4 ms to 1.2 ms, the fluid particles at the cavity mouth of the water surface still have the kinetic energy of outward diffusion, and the inner edge of the floating ice tends to overturn outward due to the fluid force. After that, the kinetic energy of the fluid particles at the water surface diffusing outward decays to zero, starting to accelerate and contract toward the middle reversely. The outer edge of the floating ice is subjected to fluid force and returns to the horizontal state (2.8 ms). The fluid continues to act on the outer edge of the floating ice, causing its inversion to the inside (4.0 ms), and the degree of inversion increases with time. Due to the relatively low projectile speed, the rise of the floating ice height is limited. In addition, the surface of the tail cavity in ice-water mixture is seriously rough and wrinkled. (0.8–2.8 ms). The reason is that the floating ice continuously disturbs the surrounding fluid during the movement, and the cavity mouth is subjected to complex and irregular impacts, so that the surface is no longer smooth and regular.

The shape of the first half of the cavity in Case 2 at 2.8 ms is the same as that in Case 1, but the second half is not elliptical and streamlined as in Case 1, instead, it is a rectangular shape with nearly the same transverse scale. According to the principle of independent expansion of the cavity cross-section, the difference in the air influx volume due to floating ice creates a difference in the conditions at the initial growth moment of the cavity cross-section from that in Case 1, resulting in a larger cavity volume in Case 2. Because the cavity in Case 2 remains connected to the outside, the difference in the size of the tail cavity between Case 1 and Case 2 becomes increasingly apparent over time. As the tail cavity gradually moves away from the floating ice, the disturbing effect of the ice on the tail cavity reduces, and the surface of the cavity gradually returns to the smooth state as in Case 1. At 6.8 ms, the oppositely contracted liquid collides below the water surface, and the surface closure occurs below the calm water surface with almost no upward jet. The floating ice is overturned and gathered, accompanied by many fine droplets splashing around.

As shown in Fig. 9, the duration of the open cavity stage is significantly longer (0.2–4.4 ms) at 400 m/s. The reason is that the higher initial speed of the projectile makes the fluid particles obtain a more incredible radial motion velocity, which causes the process of contraction toward the central axis to take longer after the kinetic energy decays to zero. Compared with 100 m/s, the cavity volume increases significantly, the water surface splashes higher, the duration of the open cavity development stage is longer, and the closure time of the cavity is delayed. The cavity shape of ice-water mixture in this stage is the same as that of only-water. There are two reasons for this: The kinetic energy of the fluid particles increases rapidly with increasing water-entry velocity, resulting in a more vital anti-interference ability of the cavity in the process of rapid formation. The other is that the ice is subjected to more substantial fluid impact to obtain a higher diffusion rate, which rapidly moves away from the water surface in a shorter period and has almost no effect on the shape of the cavity. Therefore, the surface of the tail cavity is smooth, and the cavity shape is the same for Case 5 and Case 6, which both have a “crown” splash on their liquid surfaces. The floating ice splashes hugely high along with a part of the liquid (Figs. 9b and 11b). The cavity surface closure in Case 5 occurs at 4.4 ms. However, the cavity in Case 6 still connects to the external atmospheric environment, and no surface closure forms at 7.8 ms.

3.1.2. *Difference of cavity size characteristics*

The time histories of cavity sizes at 100 m/s and 400 m/s shown in Fig. 13 are to quantitatively analyze the influence of the floating ice on the evolution of the cavity shape, including dimensionless length L_c/D_0 and dimensionless maximum diameter D_c/D_0, where L_c and D_c are the cavity length and cavity maximum diameter at the current moment.

It can be seen that the cavity lengths of Case 1 and Case 2 always remain the same throughout the water entry process with or without floating ice, which indicates that although the presence of floating ice causes differences in the duration of the open cavity stage, the cavity length is unaffected. The cavity lengths of the two cases are always the same at 400 m/s (Fig. 13c), confirming this conclusion.

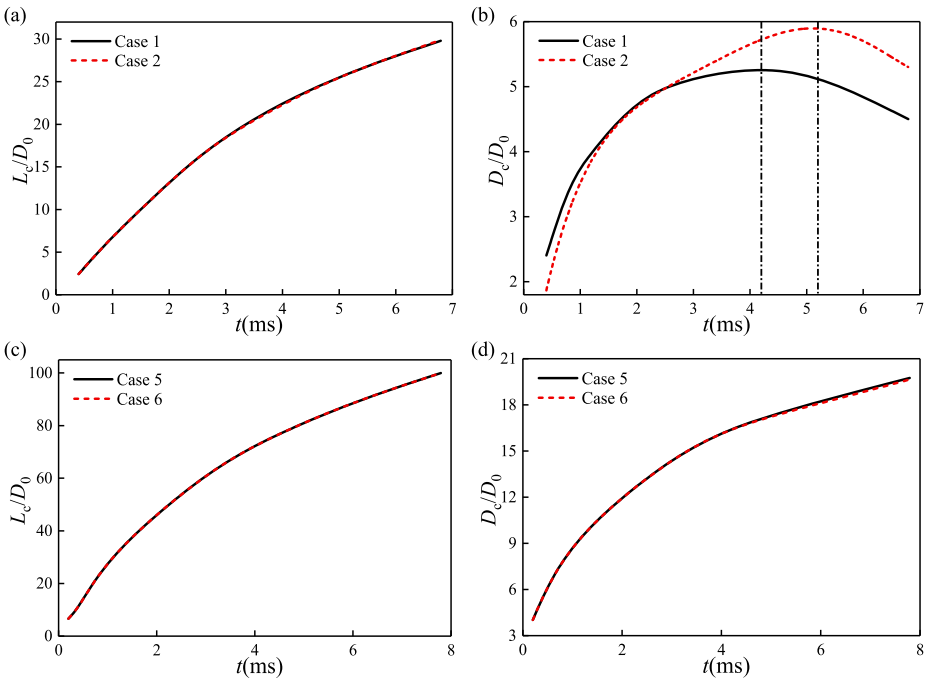

Fig. 13. Time histories of cavity sizes at 100 m/s and 400 m/s: (a) L_c/D_0 at 100 m/s, (b) D_c/D_0 at 100 m/s, (c) L_c/D_0 at 400 m/s, (d) D_c/D_0 at 400 m/s.

The dimensionless maximum diameter of the cavity in Case 1 and Case 2 is different with or without floating ice (Fig. 13). The floating ice hinders the entry of external air at the initial impact stage, causing the cavity diameter of Case 2 before 2 ms to be smaller than that of Case 1. After 2 ms, the surface closure occurs in Case 1, and the source of cavity growth only relies on vapor generated by cavitation. Nevertheless, the cavity of Case 2 still connects to the external environment, and a large amount of air continues to flow in, which results in a more significant expansion rate of the cavity diameter, causing an increasingly noticeable difference in cavity diameter between the two cases. The cavity diameter reaches the peak values at 4.2 ms and 5.2 ms in Case 1 and Case 2, respectively. Then the cavity wall begins to shrink inward due to surface tension and pressure differences inside and outside of the cavity. With the continuous elongation of the cavity by the projectile, its maximum diameter gradually decreases. It can be seen from Figs. 13c and d that there is no difference in the lateral scale of the cavity with or without floating ice at 400 m/s. Despite the difference in the external air influx, the higher velocity leads to a violent cavitation phenomenon, and the rate of vapor generation is much larger than the air influx to compensate for the difference in the air influx. Overall, the cavity length and maximum diameter during the high-speed water entry of the projectile with and without floating ice show a trend of gradual attenuation of the growth rate.

Because the shape of the water-entry cavity is approximately axisymmetric, the cavity cross-sectional area can also reflect the variation of the cavity volume law. Fig. 14 shows the cross-sectional area of the cavity on the symmetrical section in all cases. It shows that the growth rate of the cavity cross-sectional area increases with the initial water-entry velocity. The inhibitory effect of floating ice on the cavity volume growth at the early stage of water entry decreases as the projectile's initial velocity increases. At the initial impact stage, the maximum difference between the cross-sectional area of the cavity with and without floating ice is 15.3% at 100 m/s, decreasing to 9.7% at 500 m/s.

During the development of the cavity at relatively low velocities (≤200 m/s), the floating ice delays the closure time of the cavity, resulting in a larger cavity cross-sectional area than that of only-water ultimately. As the initial water-entry velocity increases, the difference in cavity cross-sectional area on the symmetric section decreases, and the influence of floating ice on the cavity volume after the initial impact can be ignored above 400 m/s.

3.2. *Influence mechanism of floating ice on the distribution of air and vapor inside the cavity*

This section analyzes the influence mechanism of floating ice on each phase fluid in the water entry process of a high-speed projectile. The above discussion shows that the floating ice significantly affects the

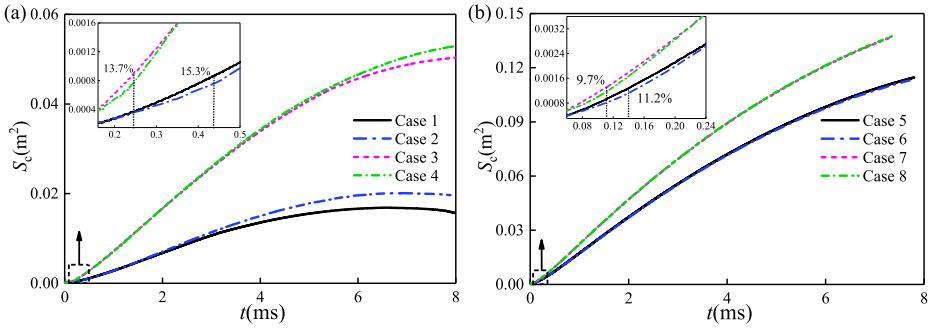

Fig. 14. Variation of the cavity cross-sectional area with time of (a) Case 1–4 and (b) Case 5–8.

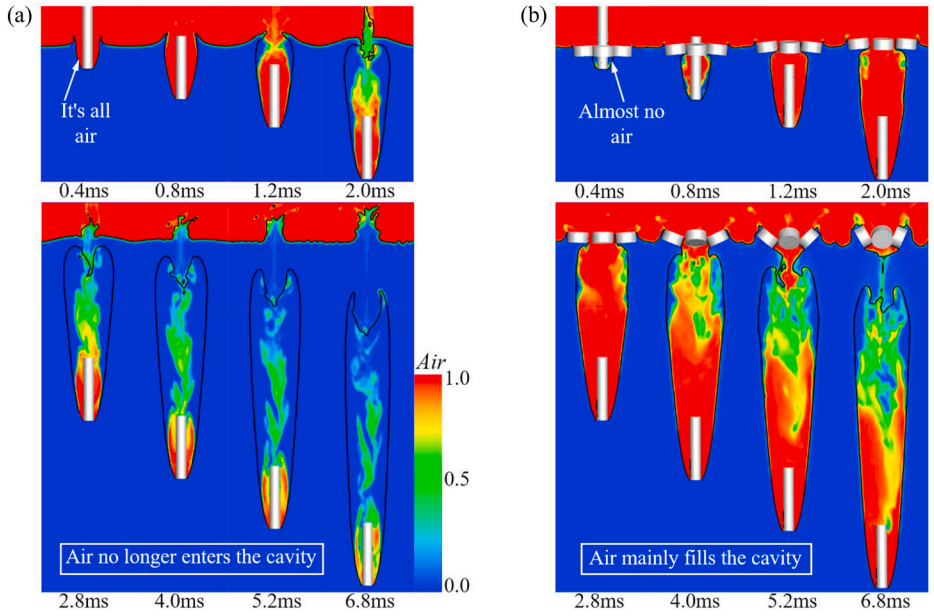

Fig. 15. Air distribution in the cavity of (a) Case 1 and (b) Case 2.

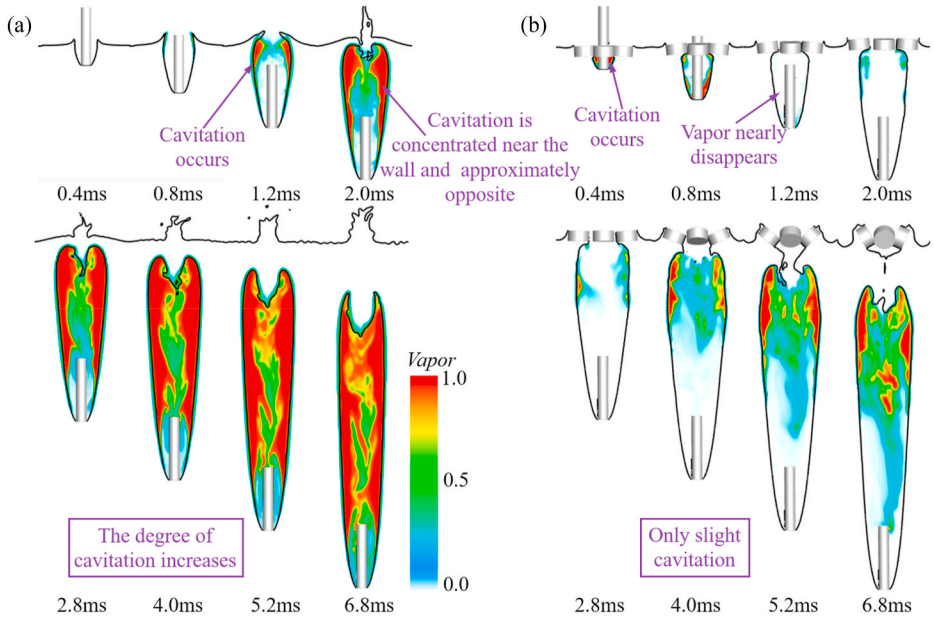

Fig. 16. Vapor distribution in the cavity of (a) Case 1 and (b) Case 2.

cavity opening time, causing a difference in the proportion of each phase fluid in the cavity, which leads to a different evolution of the cavity shape from that of only-water. Fig. 15–18 show the distribution of air and vapor with initial velocities of 100 m/s and 400 m/s, respectively.

As depicted in Figs. 15 and 16, the low-pressure area forms after the high-speed projectile impacts on the water surface, rapidly promoting air to enter the cavity at the initial impact stage (0–0.4 ms) of Case 1. It results in the internal pressure of the cavity failing to fall to the saturated vapor pressure and failing to produce cavitation. Due to the obstructing effect of floating ice in Case 2, the diffusion rate of the liquid around the projectile is much lower than that of Case 1, resulting in a slow expansion of the cavity mouth and little external air inflow. Only a tiny amount of air is carried near the projectile head. The cavitation phenomenon begins when the projectile impacts the water surface, and it is extremely evident during the initial impact stage. The vapor generated by the cavitation effect inside of the cavity at 0.4 ms occupies most of the volume (Fig. 16).

At the open cavity stage of Case 1, the diameter of the cavity mouth gradually increases, increasing the contact area between the tail cavity and the external air, and visible cavitation does not occur at the wall of the tail cavity until the cavity mouth shrinks significantly at 1.2 ms. The reason is that there is still a large amount of air around the projectile, and the contraction of the cavity mouth reduces the external air inflow rate. It results in a pressure drop to the saturated vapor pressure at the tail cavity wall away from the projectile, with the vapor distributed symmetrically along the axial. The cavitation effect intensifies with the depth of the projectile. Due to the previous influx of external air primarily concentrating on the projectile's motion path, the central axis of the cavity is dominated by air (2.0 ms).

During the formation of the open cavity in Case 2, the floating ice

gradually diffuses outwards (0.8 ms, Fig. 15b), and the proportion of the air inside of the cavity increases rapidly due to the substantial influx of external air. At 1.2 ms, the cavity mouth is much larger than that of Case 1 due to the floating ice hindering the liquid shrinkage, resulting in a large influx of air, and the cavity almost filled with air. The pressure inside of the cavity rises back up and stays above the saturated vapor pressure. The small amount of vapor generated by the cavitation effect at 0.8 ms liquefies into water (1.2 ms, Fig. 16b). There is no noticeable cavitation on the tail cavity wall until the cavity mouth shrinks at 4.0 ms. Because a large amount of high-speed moving air inside of the cavity collides with the tail of the projectile and rebounds, the scattered air disturbs the vapor generated at the cavity wall, resulting in its asymmetric distribution relative to the cavity axis.

During the cavity closure stage (2.0–6.8 ms) in Case 1, no external air enters, and the cavity grows only by cavitation. The pressure inside of the cavity gradually decreases as the cavity volume increases, further enhancing the cavitation effect, and the volume fraction occupied by vapor gradually increases. The two-phase boundary between the air and vapor at 6.8 ms is no longer as regular as that at 2.0 ms. The high-speed moving external air continuously disturbs the vapor while driving it downward, showing an apparent turbulence phenomenon (6.8 ms, Fig. 16a). At this time, the composition of the cavity in Case 2 is significantly different from that of Case 1 (Fig. 16b). Air occupies most of the cavity volume, and the vapor is distributed irregularly along the cavity wall.

As shown in Fig. 17 and Fig. 18, the cavitation effect appears earlier and more intense due to the higher initial velocity of water entry and the faster pressure drop in the cavity. In Case 5, air and vapor coexist in the initial cavity. However, under the influence of floating ice in Case 6, the inside of the cavity is full of vapor generated by the cavitation effect (0.2 ms). When the projectile passes through ice-water mixture at 400 m/s, the liquid in contact with the projectile vaporizes rapidly before it can rebound between the floating ice and the projectile. Hence, the shoulder of the projectile is not wet.

At the open cavity stage of Case 5, the formation mode of the cavity changes from almost filled by external air in Case 1 to primarily filled by vapor generated by the cavitation effect, with a tiny portion of external air. Vapor has occupied the majority of the cavity volume throughout the water-entry process. The air and vapor distribution inside of the cavity in Case 6 is significantly different from that of Case 5. After the diffusion of floating ice, the air influx is enormous, occupying the whole area surrounding the central axis of the cavity and the top of the cavity mouth. The width of the air passage is the same as the diameter of the cavity mouth. The development of the cavity mostly comes from the external air. Figs. 16b and 18b reveal that the proportion of vapor in Case 6 is more significant than in Case 2.

Fig. 19 depicts the variation of vapor volume in the cavity with time of Case 1–8. At the initial impact stage, the vapor generation rate in ice-water mixture is higher than that of only-water due to the hindrance of the floating ice. With the increase of the initial velocity, the cavitation degree increases, and the moment corresponding to the intersection of the vapor volume in ice-water mixture and only-water is advanced. The floating ice delays the cavity closure, and the external air occupies most of the cavity space, causing the total amount of vapor generated in ice-water mixture to be less than that of only-water. The growth rate of vapor gradually tends to be flat over time in each case, and the total amount of vapor increases with the initial velocity.

In summary, the initial velocity of the projectile plays an essential role in the degree of cavitation, and the floating ice alters the amount of air flowing into the cavity, which affects the degree of cavitation, the formation and development modes of the cavity, and the proportion of each phase fluid in the cavity.

3.3. *Influence of floating ice on the flow field characteristics*

Complex flow phenomena such as vortices and turbulence happen through the process of high-speed water entry of a projectile. The unsteady flow field induces the development and evolution of the cavity, which in turn will cause further changes in the characteristics of the flow field. In order to deeply study the similarities and differences in flow field characteristics during the process of a high-speed projectile entering water (without floating ice) and passing through ice-water mixture without collision with ice, the velocity field and pressure field at 100 m/s and 400 m/s, and the unsteady vortex structure dynamic characteristics were compared and discussed in Case 1 and Case 2.

3.3.1. *Distribution characteristics of the velocity field and pressure field*

The whole water-entry process of a high-speed projectile, analyzed from the energy perspective, is that the moving projectile converts the lost kinetic energy into the kinetic energy required by the fluid movement and subsequently forms the flow. The pressure and velocity distribution of the flow field are the intuitive representations of the fluid potential and kinetic energy. The velocity vector distribution on a symmetric section in Case 1 and Case 2 are shown in Fig. 20 in texture-based line integral convolution, which can visualize a large number of detailed vector fields.

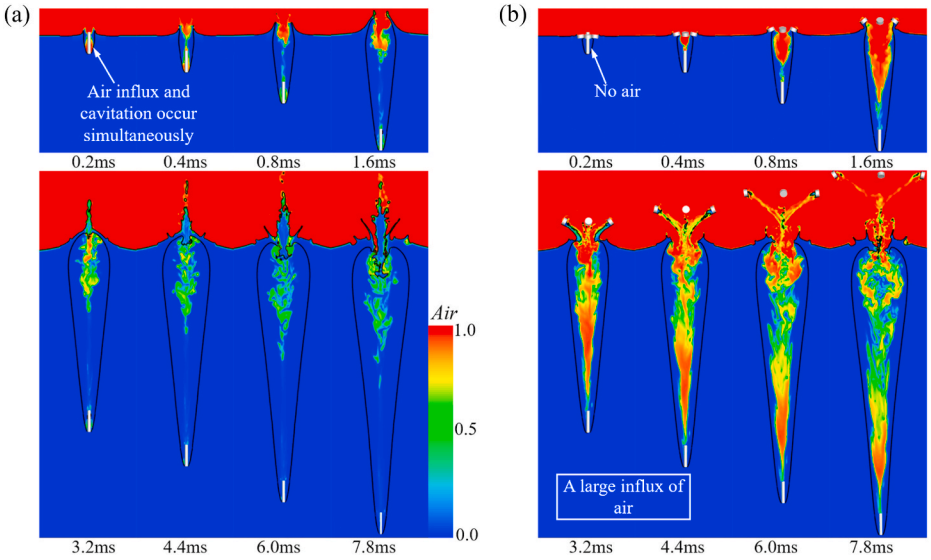

Fig. 17. Air distribution in the cavity of (a) Case 5 and (b) Case 6.

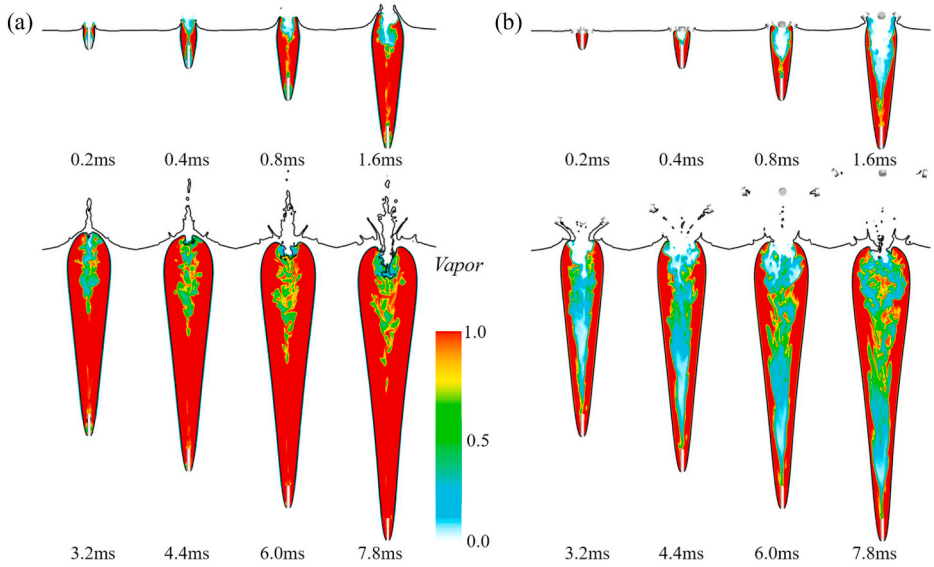

Fig. 18. Vapor distribution in the cavity of (a) Case 5 and (b) Case 6.

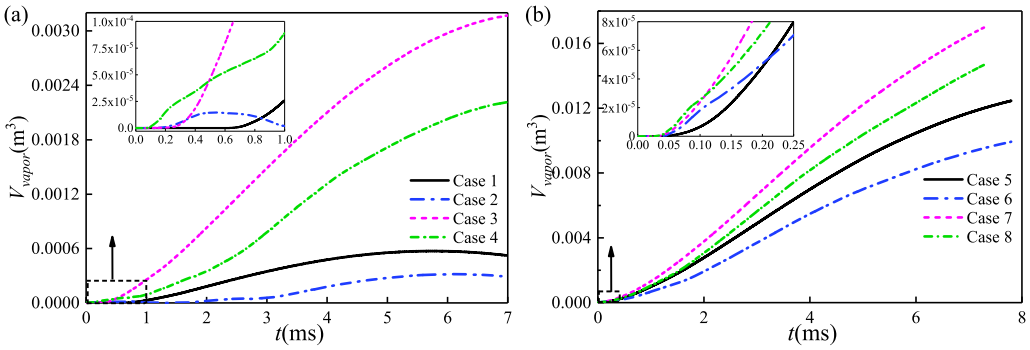

Fig. 19. The variation of vapor volume in the cavity with time of (a) Case 1–4 and (b) Case 5–8.

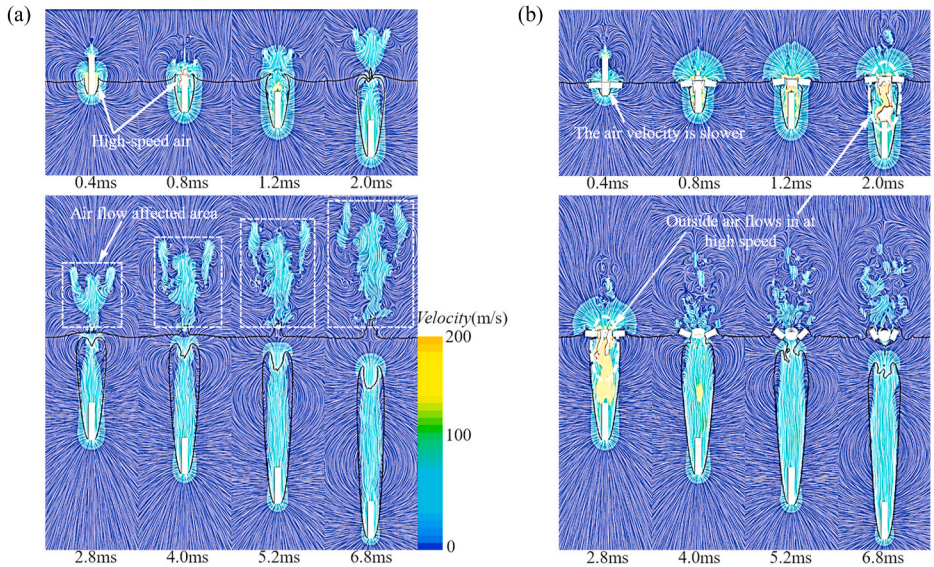

Fig. 20. Velocity distribution of (a) Case 1 and (b) Case 2.

At the initial impact stage (0–0.4 ms) of Case 1, the projectile strikes the water surface while driving the surrounding gas to move, and a high-speed area appears at the tail. After the initial cavity forms, the external air flows into the cavity at high speed, creating a visible high-speed gas flow area near the shoulder of the projectile. Comparing Figs. 20a and 20b shows that the high-speed airflow area at the initial impact stage in

Case 2 is not apparent (0.4 ms). The outside air hindered by the floating ice can only flow from the small gap between the floating ice and the projectile, resulting in a lower airflow velocity.

The liquid surface splash transfers the kinetic energy upward during the open cavity stage (0.4–2.0 ms) in Case 1, and the gas velocity near the cavity mouth gradually decreases for 0.8–2.0 ms. The area of the far-field airflow affected by the upward-splashing jet generated by surface closure continues to expand with time (2.8–6.8 ms). Combined with Figs. 15 and 16 in Section 3.2, it can be found that the higher flow velocity area in the cavity is the same as the air distribution, and the lower flow region corresponds to the vapor generation zone.

The airflow velocity distribution at the open cavity stage of Case 2 is considerably different from Case 1. The floating ice gradually spreads, and a large amount of outside air continues to flow at high speed, continuously hitting the surface of the floating ice and rebounding. As a result, even though the splashing phenomenon of the water surface in Case 2 is not apparent, there is still a high-velocity gradient above the cavity mouth. At 2.0 ms, the high-speed airflow catches up with the projectile and hits its tail. Over time, the cavity mouth gradually contracts, and the gas velocity near the water surface gradually decreases (4.0–6.8 ms). Comparing Fig. 20a and 20b, it can be seen that the airflow velocity inside of the cavity in Case 2 remains high (6.8 ms). However, the airflow velocity above the water surface is lower and the affected area of the far-field airflow is smaller.

Fig. 21 shows the pressure distribution on the symmetric cross-section of Case 1 and Case 2. A high-pressure gradient appears near the projectile head as the high-speed projectile impacts the water surface and spreads circumferentially in the form of a sphere from the contact surface of the projectile's head and water. After the initial cavity forms, air flows into the cavity at high speed, and the internal pressure of the cavity rapidly drops according to the Bernoulli principle. In a short time, the open cavity expands rapidly, and the shape of the low-pressure area is the same as the cavity.

The internal pressure of the cavity in Case 2 at 0.8 ms is at the same low level as that of Case 1, but the difference between the two cases appears at 1.2 ms. Due to the diffusion of floating ice, the external air inflow increases rapidly. Because the external environment is atmospheric pressure, the pressure drop brought by the influx of exterior air from the floating ice gap is not enough to balance the passive pressure rise caused by the large-area contact between the cavity and the outside. The internal pressure of the cavity increases and exceeds the saturated vapor pressure, resulting in a special phenomenon that the generated water vapor liquefies into water (Fig. 16b). The influx speed of air at 2.0 ms is further increased, which leads to the formation of a low-pressure area again in the flow field inside of the cavity. As the projectile penetrates deeper, its velocity continues to decay, and the area of the high-pressure zone around the projectile's head gradually decreases. The collision of the fluids moving in opposite directions forms a jet, and a high-pressure area appears at the impact point. Comparing Fig. 21a and 21b, it shows that the pressure rise at the water surface when the cavity surface closure occurs in Case 2 is weaker than that of Case 1, which reflects from the side that floating ice has a significant hindering effect on the liquid shrinkage near the cavity mouth.

Fig. 22 and Fig. 23 show the velocity and pressure distribution on the symmetric cross-section in Case 5 and Case 6. It can be seen that the airflow velocity inside of the cavity at the initial water-entry rate of 400 m/s is higher, and the area of the affected far-field airflow above the water surface is more extensive. There is still a significant difference in air velocity between cases of ice-water mixture and only-water. In Case 6, the high-speed region inside of the cavity is more pronounced, but the affected far-field airflow area is still smaller. The peak pressure around the projectile's head increases with the water-entry velocity, as shown in the pressure field in Fig. 23. There is no significant difference in the pressure distribution of the flow field with or without floating ice. It indicates that the effect of floating ice around the water-entry point on the pressure flow field can be ignored when the initial velocity of the projectile is greater than a certain critical value.

3.3.2. *Dynamic characteristics of unsteady vortex structures*

As the basic form and structure of turbulence, the vortex is the "tendon of fluid movement" (Küchemann, 1965), so the formation and evolution of vortices play a crucial role in the entire flow field. The high-speed water entry of projectiles is accompanied by cavitation, the development of which is closely linked to the vortex motion (Arakeri and Acosta, 1973; Belahadji et al., 1995). In addition, the high-speed influx of external air causes a solid disturbance to the internal flow field of the cavity, and the generation of complex vortex structures inevitably accompanies the cavity evolution. It is of great significance to

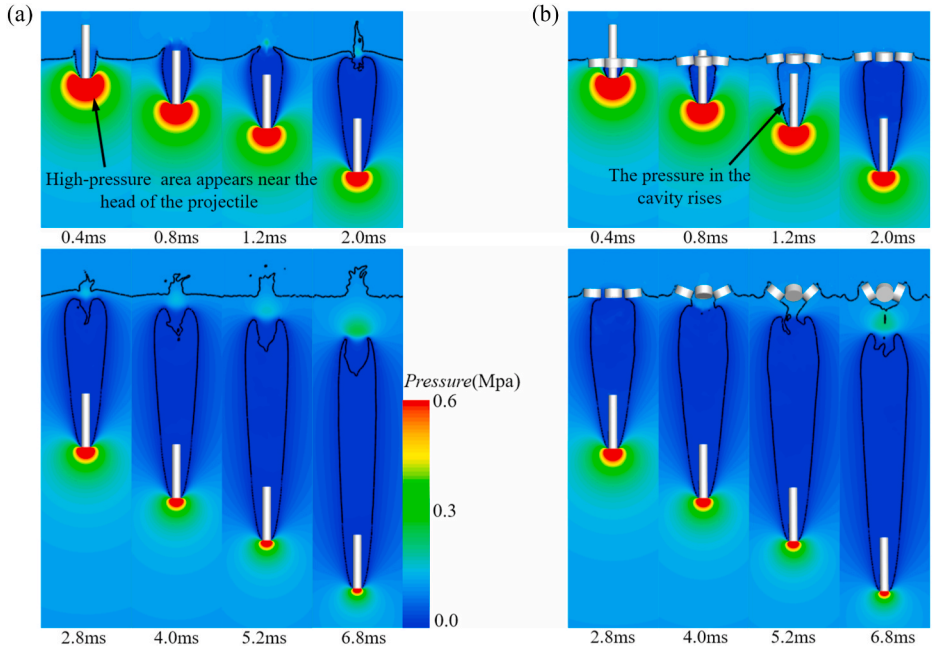

Fig. 21. Pressure distribution of (a) Case 1 and (b) Case 2.

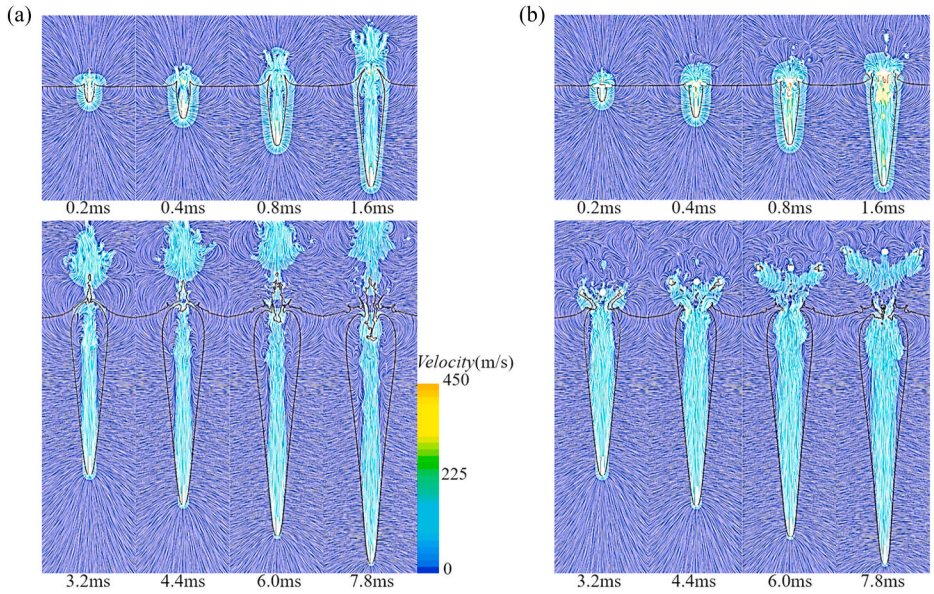

Fig. 22. Velocity distribution of (a) Case 5 and (b) Case 6.

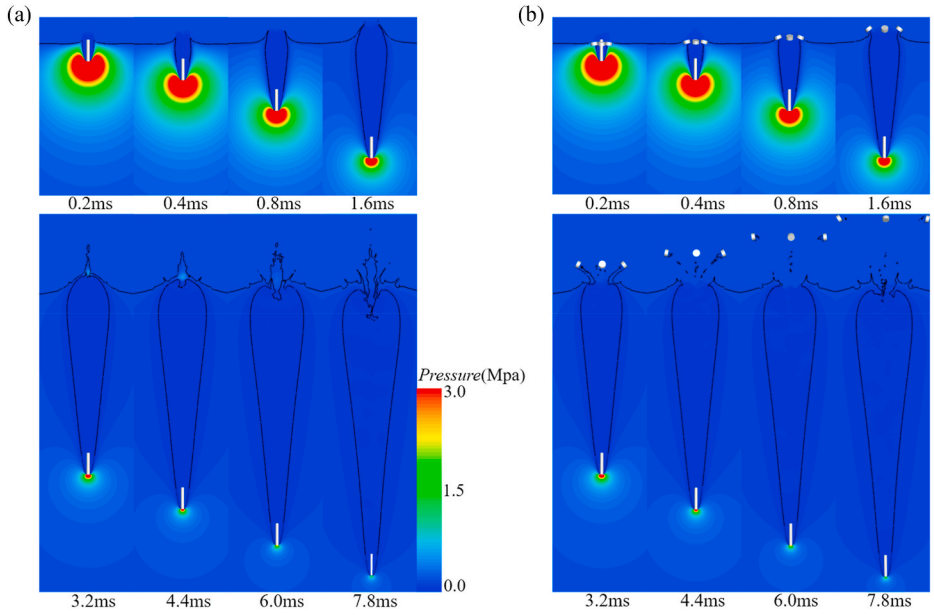

Fig. 23. Pressure distribution of (a) Case 5 and (b) Case 6.

study the dynamic characteristics of unsteady vortex structures in the cavity and near the water surface to reveal the influence mechanism of floating ice on the flow field of high-speed water entry of projectiles.

Using the Q criterion to describe vortex structures (Haller, 2005), the second invariant Q of the velocity gradient tensor under the Galilean transformation is defined as:

$$Q = \frac{1}{2}\left(\Omega^2 - S^2\right) \tag{21}$$

where $\Omega = (\partial u_i/\partial x_j - \partial u_j/\partial x_i)/2$ is the rotation tensor, $S = (\partial u_i/\partial x_j + \partial u_j/\partial x_i)/2$ is the shear strain rate tensor, $Q > 0$ means that the flow field in the region is dominated by vortices; $Q < 0$ means that the shear deformation effect is predominant.

According to section 3.3.1, the difference of flow field with or without floating ice decreases with the increase of initial water-entry velocity. Therefore, only compare and analyze the unsteady vortex structure dynamic characteristics with noticeable differences in Case 1 and Case 2. Fig. 24 shows the vortex distribution of the symmetrical section at different moments in Case 1 and Case 2, which is combined with the velocity vector field in Fig. 20 for comparative analysis.

During the initial impact stage (0–0.4 ms) of Case 1, the fluid particles around the initial cavity are subjected to strong shear deformation, resulting in a significant negative Q region, while only a tiny positive Q region near the initial splash and the projectile's tail. The vortices are symmetrically distributed around the projectile's rotation axis in opposite directions (Fig. 20). In contrast to Case 1, the shoulder of the projectile also has an obvious positive Q region at 0.4 ms in Case 2. The reason is that part of the air hits the surface of the floating ice and then bounces back to the projectile wall during the influx of external air into the initial cavity, which is "rolled" into a vortex after friction with the wall.

At the open cavity stage in Case 1, the influx of external air rises, and

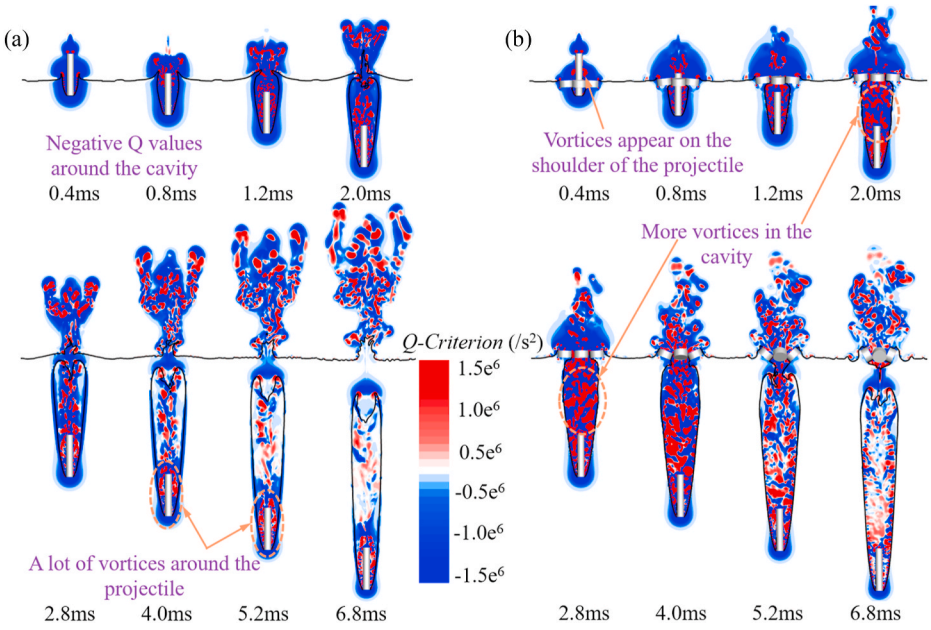

Fig. 24. Vortex distribution on the symmetrical section of (a) Case 1 and (b) Case 2.

a large number of multiscale vortices appear in the cavity (1.2 ms), and the number of vortices further increases with time (2.0 ms). The cavity wall surrounds by a wide negative Q value area, which indicates that the cavity wall, especially near the projectile's head, is dominated by the shear deformation effect. The positive and negative Q-value areas inside of the cavity are alternately distributed, indicating that the shear deformation and rotation effects jointly dominate the flow inside of the cavity. At the same time, a large area of negative Q value appears near the surface closure due to the strong interaction caused by the collision of liquid contraction. The upward jet further pushes the vortices formed by the airflow above the water surface to spread farther. The vortices in this region show a symmetric rotation effect along the axis of the projectile (2.8 ms, Fig. 20a). The velocity of the projectile drops as it penetrates, the area of negative Q value near its head diminishes gradually, and the strength of shear deformation decreases. Due to no external energy replenishment after surface closure and continuous energy consumption during motion, the vortices inside of the cavity have diminished in intensity and number (6.8 ms). Most of the vortices are concentrated around the projectile and are dominated by solid shearing action, moving downward with the projectile.

Figs. 24a and 24b show that the dynamic characteristics of vortex structures in the flow field of Case 2 during the cavity development are quite different from those of only-water. The area with negative Q values above the water surface is more extensive (0.8 ms), and the shear deformation effect of the flow field in this area is more potent because the floating ice hinders the airflow. Due to the floating ice hindering the

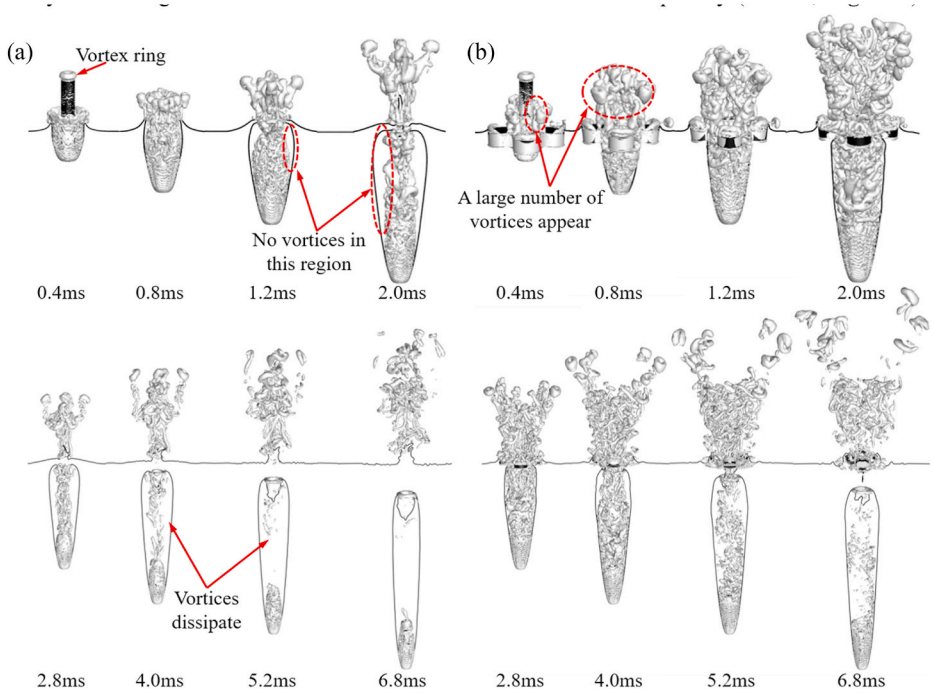

Fig. 25. Vortex distribution in three-dimensional space of (a) Case 1 and (b) Case 2.

contraction of the cavity mouth and the continuous high-speed influx of external air, more vortices with greater intensity (2.0 ms) occur in the cavity. Vortex and deformation effects fill the whole cavity and distribute more densely, resulting in more complex characteristics of the cavity flow field in ice-water mixture. Due to the larger airflow with higher velocity, the scale of the vortices inside of the cavity is greater (2.8–4.0 ms). Large-scale vortices reach saturation and then gradually destabilize and separate due to mutual stretching mechanisms, breaking into a large number of irregular small-scale vortices (5.2 ms). After the surface closure, many vortices remain in the cavity (6.8 ms).

It can be seen from the whole evolution process of the cavity that the generation, development, coupling, motion, destabilization, separation, and dissipation of the vortex structures show strong non-stationarity, and the rotation and shear deformation effects jointly dominate the generation and development of the cavity.

The two-dimensional distribution of vortices is insufficient to reveal their three-dimensional characteristics ultimately. Fig. 25 shows the variation of the vortex structures with time in three-dimensional space with an isosurface of Q=1500000 s^{-2}.

At the initial impact stage, due to the high-speed gradient of the projectile tail, a vortex ring connected end to end parallel to the projectile tail occurs in both cases (0.4 ms, Fig. 25), which is centered on the projectile's rotation axis and symmetrically distributed in horizontal and vertical directions. However, the quantity and strength of the vortices around the projectile in the two cases differ significantly. The high-speed air obstructed by the floating ice interacts with the projectile wall, resulting in a more turbulent airflow surrounding the projectile. After stretching and rotating the airflow, a significant number of irregular vortex structures occur in this area, and the vortices cover most of the projectile. However, the vortices only exist near the shoulder of the projectile in only-water.

At the open cavity stage, vortex stretching and baroclinic moments dominate the development of the flow field. Combined with the velocity vector field in Fig. 20, it can be seen that the external air flows into the cavity at high speed during the development of the cavity, generating high-speed and high-pressure gradients, resulting in the generation of a large number of vortices. The vortex ring separates and disappears under the action of the flow impact (0.8 ms, Fig. 25). Combining with Figs. 15 and 16, it can be found that the vortices are located in the area where the outside air is. The location of the vapor generated by the cavitation effect has almost no vortex generation, indicating that the vortices are primarily generated in the region where the external air flows at high speed. In Case 1, a vast number of vortices in the cavity following the surface closure dissipates and disappears, leaving just a small number of vortices existing around the projectile (2.8–6.8 ms, Fig. 25a). Because the outside air in Case 2 occupies most of the volume of the cavity, the vortices almost fill the entire cavity space (1.2–2.8 ms, Fig. 25b). At 6.8 ms, vortex dissipation also occurs after surface closure. However, the quantity of vortices in the cavity is still greater than that of Case 1.

As for the development of vortices above the water surface, the vortices in Case 1 mainly move vertically upward, and the number and intensity of vortices have hardly attenuated during the whole movement (2.8–6.8 ms, Fig. 25a). This can be attributed to the upward-moving jet generated by surface closure continuously providing the energy required for the motion of vortices. Vortices are constantly generated near the jet and move upward. Due to the interaction between the outside air and the floating ice, the strength and number of the vortices above the water surface do not decay before the cavity surface closure of Case 2. However, many vortices move to both sides during the upward development process, showing "a funnel-shape". The reason is that the tail cavity mouth remains connected to the outside, and the high-speed influx of external air drives the development of vortices and disperses them. Due to the lack of energy supplementation by the jet, nearly no new vortices generate near the floating ice following the surface closure. The quantity and strength of vortices above the water surface decrease quickly (6.8 ms, Fig. 25b).

3.4. Influence of floating ice on the hydrodynamic and ballistic characteristics of the projectile

In order to further study the influence of floating ice on the hydrodynamic characteristics of the projectile with different initial velocities in the process of entering water, Fig. 26 shows the vertical drag force and drag coefficient curves of the projectile for all the cases. Fig. 27 shows the horizontal drag force curves. The resistance coefficient is treated dimensionless as follows:

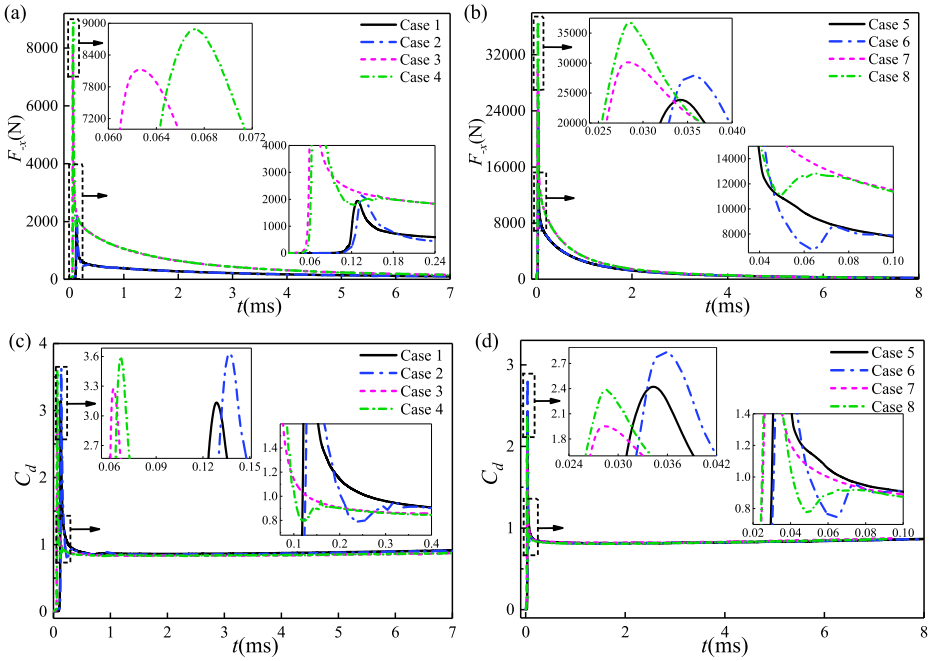

Fig. 26. Vertical drag force and drag coefficient curves of the projectile: (a) F_{-x} of Case 1–4, (b) F_{-x} of Case 5–8, (c) C_d of Case 1–4, (d) C_d of Case 5–8.

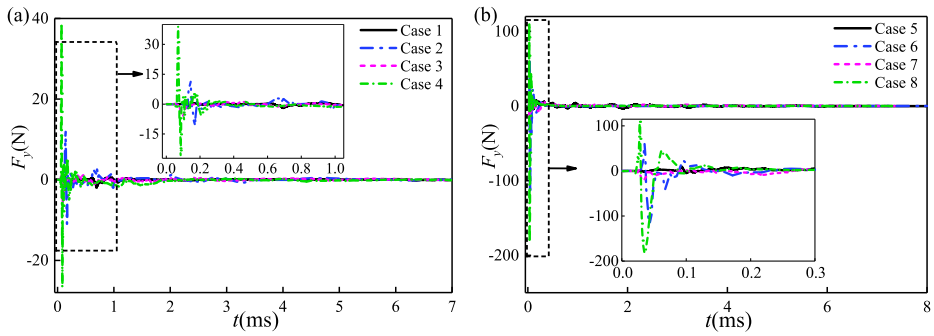

Fig. 27. Horizontal drag force curves of the projectile of (a) Case 1–4 and (b) Case 5–8.

$$C_d = \frac{F_{-x}}{0.5\rho_l v^2 S} \tag{22}$$

where F_{-x} is the vertical drag force of the projectile, S is the characteristic area of the projectile, $S = \pi D_0{}^2/4$, v is the moving speed of the projectile.

At the initial impact stage, the projectile's head substantially impacts the water surface, and the drag forces in both directions and the vertical drag coefficient reach a peak at the moment of entering the water. After the formation of the open cavity, the drag force decreases rapidly due to the attenuation of the impact effect. With the increase of the initial velocity of the projectile, the greater the peaks of drag force in the vertical and horizontal directions, the smaller the peak drag coefficient, and the appearance time of the peaks is earlier.

The peak value of drag force in the vertical direction of the projectile passing through ice-water mixture is higher than that of only-water, and the peak occurs slightly later. The drag force on the projectile and the drag coefficient fluctuate during a rapid decline, while those of only-water keep a smooth decline (Fig. 26). In addition, the horizontal drag in ice-water mixture presents alternating loads significantly greater than that of only-water at the initial impact stage (Fig. 27). The reason for this is that in the process of the projectile impacting the water surface, the floating ice is solid, and its inertia is much larger than that of water. At this time, floating ice is equivalent to increasing the viscosity of the fluid at the air-water interface, resulting in an increase in the peak force in the vertical direction of the projectile and a delay in the peak appearance time. Moreover, the continuous interaction of projectile-water-ice causes the projectile to be disturbed much more violently than only-water, resulting in a violent fluctuation of the drag force curve.

After the floating ice has spread out to a certain distance from the projectile, the disturbance of the ice to the projectile gradually decreases, and the drag force curves in both directions gradually overlap with those of only-water. It can be seen that the influence of ice-water mixture on the drag forces of the projectile into water at high speed is mainly concentrated at the initial impact stage. The drag coefficients of the projectile at different initial speeds tend to have a constant value after entering a certain depth of water, which are stable at about 0.85. It shows that the drag coefficient of steady-state navigation is independent of speed and floating ice when the same projectile enters the water vertically at different initial speeds.

Fig. 28a and Fig. 28b show the velocity curves in the vertical and horizontal directions of Case 1–8, respectively. The projectile's velocity decay rate increases with the initial water-entry velocity increase because the fluid force of the projectile is proportional to the square of the velocity. The nonlinear trend of velocity decay also becomes more evident with the increase of initial velocity. The projectile's velocity decreases continuously in the penetration process, and the drag force and the velocity attenuation rate in the vertical direction decrease

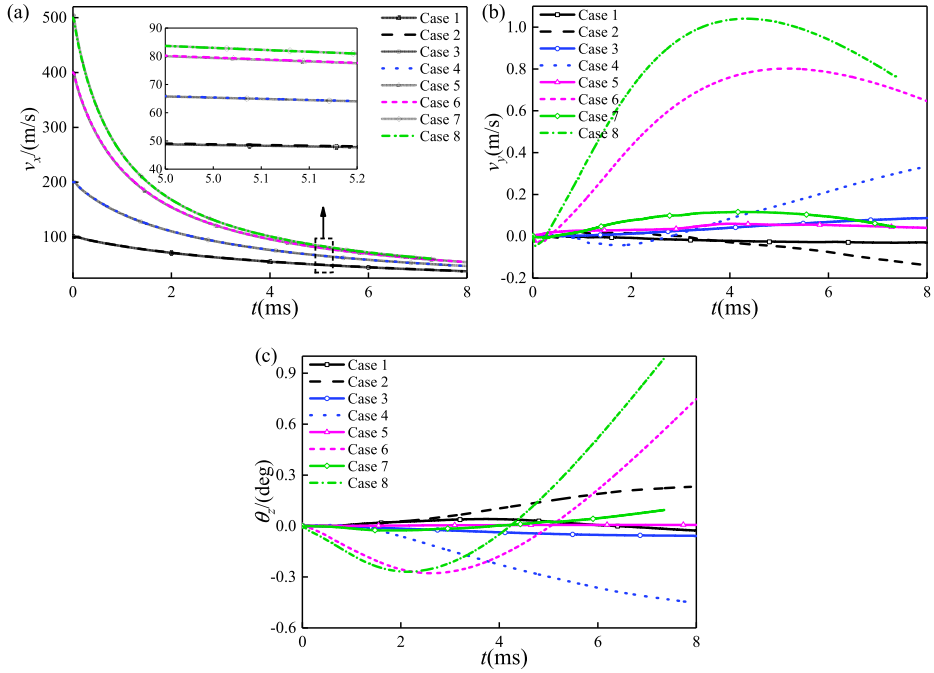

Fig. 28. Ballistic characteristics of the projectile of Case 1–8: (a) Vertical velocity, (b) Horizontal velocity, (c) Pitch angle displacement in the z-direction.

gradually. The variation trend of projectile velocity in the vertical direction in ice-water mixture and only-water is the same. The horizontal velocity of the projectile is almost zero in only-water. Affected by the disturbance of floating ice, the horizontal velocity of the projectile with the same initial velocity in ice-water mixture is much larger than that of only-water, and the difference with only-water increases with the initial velocity.

Fig. 28c depicts the pitch angle displacement in the z-direction of the projectile during the water entry. The degree of pitch deflection increases with the initial velocity of water entry because the alternating load on the horizontal direction of the projectile during the initial impact stage becomes more intense with the higher initial velocity (Fig. 27), resulting in a greater deflection of the projectile. The ballistic characteristics of the projectile are more stable in only-water, but the alternating load at the initial impact stage in ice-water mixture is much more severe than that of only-water, resulting in a large deflection of the pitch angle. It can be seen that the floating ice has a particular influence on the horizontal speed and pitch angle of the projectile after entering water at high speed, which makes the trajectory of the projectile deflect greatly after entering water.

4. Conclusions

In this paper, the processes of a high-speed projectile vertically entering water (without floating ice) and passing through ice-water mixture without collision with ice at different initial velocities were comparatively investigated. The influence mechanism of floating ice on the evolution of the water-entry cavity shape and the proportion of each phase fluid in the cavity was analyzed. At the same time, the influences of floating ice on the characteristics of flow fields, hydrodynamic and ballistic characteristics of the projectile were deeply discussed. The main findings can be summarized as follows:

During the process of the high-speed projectile vertically passing through ice-water mixture, the floating ice alters the air inflow by hindering the liquid diffusion and contraction movement at the gas-liquid interface, changing the cavitation degree and the formation and development modes of the cavity. It causes a different evolution of the cavity shape, delays the cavity closure, and affects the hydrodynamic force and ballistic characteristics of the projectile ultimately. With increasing velocity, the influence of ice on cavity shape reduces, however, on projectile ballistics, it enhances. The floating ice obviously influences the water-entry cavity shape of the projectile at 100 m/s. For example, the shoulder of the projectile is wet, the liquid splash phenomenon has changed, and the surface of the tail cavity is approximately rectangular and wrinkled. Moreover, the surface closure point moves below the calm water surface. There is almost no upward jet, and the cavity volume is significantly larger. The influence of floating ice on the volume of the water-entry cavity can be neglected when the projectile's initial velocity is greater than 400 m/s.

Floating ice greatly increases the air flowing into the cavity and weakens the cavitation effect, thereby changing the proportion of each phase fluid in the cavity. The gas flow rate inside of the cavity in ice-water mixture is higher, but the affected area of the far-field gas flow above the liquid surface is smaller. The floating ice increases the quantity and size of vortices in the cavity, changes the trajectory of the vortices above the liquid surface, and makes them dissipate earlier. The vortex structure and shear deformation effect dominate the flow inside of the cavity. The continuous interaction of projectile-water-ice causes the projectile to be disturbed much more violently than that of only-water during the initial impact stage. The floating ice makes the trajectory of the projectile deflect greatly after enteringwater, and the influence of the floating ice on the horizontal velocity and pitch angle of the projectile increases with initial velocity.

CRediT authorship contribution statement

Hao Wang: Investigation, Software, Formal analysis, Conceptualization, Methodology, Writing – original draft, Writing – review & editing. **Zhengui Huang:** Conceptualization, Formal analysis, Writing – Reviewing and Editing, Supervision. **Ding Huang:** Investigation, Editing. **Yu Hou:** Methodology, Validation. **Zhihua Chen:** Conceptualization, Supervision, Visualization. **Zeqing Guo:** Software, Data curation. **Shuai Sun:** Giving a good advice in the cavity evolution. **Renyuxin Xue:** Graphic.

Declaration of competing interest

The authors declare that they have no known competing financial interests or personal relationships that could have appeared to influence the work reported in this paper.

Data availability

The authors are unable or have chosen not to specify which data has been used.

Acknowledgments

This research is supported by the National Natural Science Foundation of China (No. 12002165), the Major Basic Research Project and Quick Support (80907020304) of Equipment Development Department, Nature Science Youth Foundation of Jiangsu Province (No. BK20210348), and National Key laboratory Foundation of Transient Physics (No. 6142604210603). We are grateful for their support. In addition, We are appreciate Yan Doudou support on proving the English academics and accuracy of this paper.

References

Arakeri, V.H., Acosta, A.J., 1973. Viscous effects in the inception of cavitation on axisymmetric bodies. J. Fluid Eng. 95 (4), 519–527.
Belahadji, B., Franc, J.P., Michel, J.M., 1995. Cavitation in the rotational structures of a turbulent wake. J. Fluid Mech. 287, 383–403.
Cai, X.W., Xuan, J.M., Wang, B.S., Li, W., Zhang, J., 2020. Numerical simulation of thin body passing through the ice-water mixture flow field. Acta Armamentarii. 41 (S1), 79–90.
Chen, C., Yuan, X.L., Liu, X.Y., Dang, J.J., 2019a. Experimental and numerical study on the oblique water-entry impact of a cavitating vehicle with a disk cavitator. Int. J Nav Arch Ocean. 11 (1), 482–494.
Chen, T.T., Chen, X.E., 2021. Numerical simulation of sea ice in Bohai Sea in winter of 2012–2013. Trans. Oceanol. Limnol. 43, 1–10.
Chen, T., Huang, W., Zhang, W., Qi, Y.F., Guo, Z.T., 2019b. Experimental investigation on trajectory stability of high-speed water entry projectiles. Ocean Eng 175, 16–24.
Haller, G., 2005. An objective definition of a vortex. J. Fluid Mech. 525, 1–26.
Hou, Y., Huang, Z.G., Guo, Z.Q., Chen, Z.H., Liu, R.S., Luo, Y.C., 2020. Experimental investigation on shallow-angle oblique water-entry of a high-speed supercavitating projectile. Acta Armamentarii. 41 (2), 332–341.
Hou, Z., Sun, T.Z., Quan, X.B., Zhang, G.Y., Sun, Z., Zong, Z., 2018. Large eddy simulation and experimental investigation on the cavity dynamics and vortex evolution for oblique water entry of a cylinder. Appl. Ocean Res. 81, 76–92.
Huang, B., Young, Y.L., Wang, G.Y., Shyy, W., 2013. Combined experimental and computational investigation of unsteady structure of sheet/cloud cavitation. J. Fluid Eng. 135 (7), 071301.
Jiang, C.X., Li, F.C., 2014. Experimental and numerical study of water entry supercavity influenced by turbulent drag-reducing additives. Adv. Mech. Eng. M.
Jiang, C.X., Shuai, Z.J., Zhang, X.Y., Li, W.Y., Li, F.C., 2016. Numerical study on the transient behavior of water-entry supercavitating flow around a cylindrical projectile influenced by turbulent drag-reducing additives. Appl. Therm. Eng. 104, 450–460.
Kirschner, I.N., Kring, D.C., Stokes, A.W., Fine, N.E., Uhlman, J.S., 2002. Control strategies for supercavitating vehicles. J. Vib. Control 219–242.
Küchemann, D., 1965. Report on the I.U.T.A.M. symposium on concentrated vortex motions in fluids. J. Fluid Mech. 21, 1–20.
Lee, M., Longoria, R.G., Wilson, D.E., 1997. Cavity dynamics in high-speed water entry. Phys. Fluids 9, 540–550.
Logvinovich, G.V., 1969. Hydrodynamics of Flows with Free Boundaries. Naukova Dumka, Kiev.
Lu, L., Wang, C., Li, Q., Sahoo, P.K., 2021. Numerical investigation of water-entry characteristics of high-speed parallel projectiles. Int. J Nav Arch Ocean. 13, 450–465.

Lyu, X.J., Yun, H.L., Wei, Z.Y., 2021. Influence of time interval on the water entry of two spheres in tandem configuration. Exp Fluids. 62 (11), 1–9.
Lyu, X.J., Wang, X., Yun, H.L., Chen, Z.H., 2022. On water-entry modes of the latter sphere in tandem configuration with two spheres. J. Fluid Struct. 112, 103601.
Menter, F.R., 1994. Two-equation eddy-viscosity turbulence models for engineering applications. AIAA J. 32 (8), 1598–1605.
Mirzaei, M., Taghvaei, H., Alishahi, M.M., 2020a. Mathematical modeling of the oblique water-entry of cylindrical projectiles. Ocean Eng. 205, 107257.
Mirzaei, M., Taghvaei, H., Golneshan, A.A., 2020b. Improvement of cavity shape modeling in water-entry of circular cylinders by considering the cavity memory effect. Appl. Ocean Res. 97, 1–11.
Mu, Q., Xiong, T.X., Wang, K.J., Yi, W.J., Guan, J., 2020. Numerical simulation on the cavitation flow of high speed oblique water entry of revolution body with different density. Acta Armamentarii. 41 (S1), 116–121.
Nam, J.H., Park, I., Lee, H.J., Kwon, M.O., Choi, K., Seo, Y., 2013. Simulation of optimal Arctic routes using a numerical sea ice model based on an ice-coupled ocean circulation method. Int. J Nav Arch Ocean. 5 (2), 210–226.
Rand, R., Pratap, R., Ramani, D., Cipolla, J., Kirschner, I., 1997. Impact dynamics of a supercavitating underwater projectile. In: Proceedings of the 1997 ASME Design Engineering Technical Conferences. Sacramento, CA, US.
Ren, H.F., Zhao, X., 2021. Numerical simulation for ice breaking and water entry of sphere. Ocean Eng 243, 110198.
Rokaya, P., Budhathoki, S., Lindenschmidt, K., 2018. Ice-jam flood research: a scoping review. Nat. Hazards 94, 1439–1457.
Sui, Y.T., Zhang, A.M., Ming, F.R., Li, S., 2021. Experimental investigation of oblique water entry of high-speed truncated cone projectiles: cavity dynamics and impact load. J. Fluid Struct. 104, 103305.
Schnerr, G.H., Sauer, J., 2001. Physical and Numerical Modeling of Unsteady Cavitation Dynamics. C. ICMF-2001 International Conference on Multiphase Flow.
Toyota, T., Haas, C., Tamura, T., 2011. Size distribution and shape small sea-ice floes in the Antarctic marginal ice zone in properties of relatively late winter. DEEP-SEA RES PT II 58 (9–10), 1182–1193.
Truscott, T.T., Epps, B.P., Belden, J., 2014. Water entry of projectiles. Annu. Rev. Fluid Mech. 46, 355–378.
Truscott, T.T., Techet, A., Beal, D., 2009. Shallow angle water entry of ballistic projectiles. In: 7th International Symposium on Cavitation, pp. 1–14.
Wang, H., Luo, Y.C., Chen, Z.H., Guo, Z.Q., Huang, Z.G., 2022. Influences of ice-water mixture on the vertical water-entry of a cylinder at a low velocity. Ocean Eng. 256, 11464.
Wang, Q.K., Li, Z.J., Lu, P., Lei, R.B., Cheng, B., 2018. 2014 summer Arctic sea ice thickness and concentration from shipborne observations. Int. J. Digit. Earth 12 (8), 931–947.
Wu, J.Y., Wang, G.Y., Shyy, W., 2005. Time-dependent turbulent cavitating ow computations with interfacial transport and lter-based models. Int. J. Numer. Methods Fluid. 49 (7), 739–761.
You, C., Sun, T.Z., Zhang, G.Y., Wei, Y.J., Zong, Z., 2022. Numerical study on effect of brash ice on water exit dynamics of ventilated cavitation cylinder. Ocean Eng. 245, 110443.
Zhang, G.Y., You, C., Wei, H.P., Sun, T.Z., Yang, B.Y., 2021. Experimental study on the effects of brash ice on the water-exit dynamics of an underwater vehicle. Appl. Ocean Res. 117, 102948.
Zhang, J., Cai, X.W., Xuan, J.M., Wang, Y.L., 2020. Numerical simulation of flow field of projectile passing through ice water mixture. J. Ballist. 32, 35–40.
Zhao, C.G., Wang, C., Wei, Y.J., Zhang, X.S., Sun, T.Z., 2016. Experimental study on oblique water entry of projectiles. Modern. Phys. Lett. B30 (28), 1650348.
Zhao, J.P., Cao, Y., Shi, J.X., 2006. Core region of Arctic Oscillation and the main atmospheric events impact on the Arctic. Geophys. Res. Lett. 33 (22), L22708.